High-velocity impact fragmentation of additively-manufactured metallic tubes

J. C. Nieto-Fuentes[a,*], J. Espinoza[b], F. Sket[b], J. A. Rodríguez-Martínez[a]

[a]*Department of Continuum Mechanics and Structural Analysis. University Carlos III of Madrid. Avda. de la Universidad, 30. 28911 Leganés, Madrid, Spain*
[b]*IMDEA Materials Institute, c/Eric Kandel 2, 28906, Getafe, Madrid, Spain*

Abstract

In this paper, we have developed and demonstrated a novel high-velocity impact experiment to study dynamic fragmentation of additively-manufactured metals. The experiment consists of a light-gas gun that fires a conical nosed cylindrical projectile that impacts axially on a thin-walled cylindrical tube fabricated by 3D printing. The diameter of the cylindrical part of the projectile is approximately twice greater than the inner diameter of the cylindrical target, which is expanded as the projectile moves forward, and eventually breaks into fragments. The experiments have been performed for impact velocities ranging from ≈ 180 m/s to ≈ 390 m/s, leading to strain rates in the cylindrical target that vary between ≈ 9000 s^{-1} and ≈ 23500 s^{-1}. The cylindrical samples tested are printed by Selective Laser Melting out of aluminium alloy AlSi10Mg, using two printing qualities, with two different outer diameters, 12 mm and 14 mm, and two different wall thicknesses, 1 mm and 2 mm. A salient feature of this work is that we have characterized by X-ray tomography the porous microstructure of selected specimens before testing. Three-dimensional analysis of the tomograms has shown that the initial void volume fraction of the printed cylinders varies between 1.9% and 6.1%, and the maximum equivalent diameter of the 10 largest pores ranges from 143 µm to 216 µm, for the two different printing conditions. Two high-speed cameras have been used to film the experiments and thus to obtain time-resolved information on the mechanics of formation and propagation of fractures. Moreover, fragments ejected from the samples have been recovered, sized, weighted and analyzed using X-ray tomography, so that we have obtained indications on the effect of porous microstructure, specimen dimensions and loading velocity on the number and distribution of fragment sizes. To the authors' knowledge, this is the first paper ever (i) providing a systematic experimental study (34 impact tests) on the fragmentation behavior of printed specimens, and (ii) including 3D reconstructions of dynamic cracks in porous additively-manufactured materials.

Keywords:
High-velocity impact, Axial penetration, Fragmentation, Additively-manufactured metals, X-ray tomography

*Corresponding author. Tel. +34 916249588, E-mail address: junietof@ing.uc3m.es

1. Introduction

The ring expansion test developed by Niordson (1965) was a turning point in the experimental research on dynamic localization and fragmentation of metallic materials. In this impact experiment, a circular ring specimen is expanded at large velocities up to two or three hundreds of meters per second by detonation of an explosive charge (Diep et al., 2004) or by application of transient magnetic fields (Grady and Benson, 1983; Altynova et al., 1996; Zhang and Ravi-Chandar, 2006). While the magnetic loading technique has become more popular, largely because it is more conducive to a laboratory environment than explosive loading schemes, and loading rates are readily controlled trough variation of the driving current pulse, it shows the drawback that, since it is based on the principle of opposing forces between primary and induced currents, Joule heating effects occur in the sample material. The strain rates attained in the electromagnetic loading ring expansion experiments generally range from $5 \cdot 10^3$ s^{-1} to $5 \cdot 10^4$ s^{-1}, for specimens with diameter typically varying between 27 mm and 36 mm. For thin rings, the radial stress becomes negligible in comparison with the circumferential stress, so that the stress field is mainly uniaxial. In addition, the symmetry of the problem nearly eliminates the effects of wave propagation along the circumferential direction of the specimen, so that the material stretches during loading until homogeneous deformation fails at large strain, leading to the nucleation of multiple necks –in ductile materials– and subsequent fragmentation.

Since the pioneering work of Niordson (1965), only few laboratories have mastered the ring expansion testing technique. For instance, Grady and co-workers (Grady and Benson, 1983; Grady and Olsen, 2003) performed experiments with OFHC copper, aluminum 1100–O and U6N specimens, with $30 - 32$ mm in diameter and $0.75 - 1$ mm in thickness of square cross section, expanding to radial velocities ranging over $50 - 300$ m/s. The experiments revealed that the fracture strain of the specimens, the number of necks and the number of fragments all increase with the expansion velocity, the number of fragments being less than the number of necks. Following the concepts of fragmentation statistics put forth by Mott (1947), Grady and Benson (1983) stated that the arrested necks result from the arrival of relieving stress waves from a nearby fractures that remove the driving force before fracture is completed. Moreover, Altynova et al. (1996) carried out ring expansion tests with solutionized Al6061, Al6061–T6, and OFHC Cu specimens, with similar dimensions to the samples used by Grady and Benson (1983), and tested within the same range of radial velocities. Altynova et al. (1996) reported that the strains to failure of the three materials increase continuously with increasing velocity, and attributed the increase in ductility to inertia and changes in material constitutive behavior at high strain rates. As Molinari and collaborators would later confirm using perturbation analyses (Fressengeas and Molinari, 1985, 1994; Mercier and Molinari, 2003, 2004), inertia affects ductility because the necking development is impeded due to the circumferential acceleration that stabilizes plastic flow and opposes to localization. Altynova et al. (1996) showed that at expansion velocities greater than 200 m/s the ductility of the samples exceed the quasi-static value by 60, 150, and 250% for OFHC Cu, solutionized Al6061, and Al6061–T6, respectively. Years later, Zhang and Ravi-Chandar (2006) performed ring expansion experiments using Al6061–O specimens with rectangular cross section of thickness 0.5 mm and length of 1 mm, at velocities ranging from 80 to 200 m/s, and photographed the tests using a high-speed camera obtaining time-resolved images of the necking and fragmentation processes. Consistent with the earlier results of Grady and co-workers (Grady and Benson, 1983; Grady and Olsen, 2003) and Altynova et al. (1996), the experiments of Zhang and Ravi-Chandar (2006) showed that the number of necks and fragments increases rapidly with the expanding speed of the ring, and that the resulting distributions of neck and fragment sizes are governed by the statistical material property and microstructure variations (which activate the nucleation of necks in specific locations), and by the propagation of the unloading or release waves from early growing necks and fractures. Shortly after, Zhang and Ravi-Chandar (2008) published additional ring expansion experiments with samples of the same size made of Al1100–H14 and Cu101. The tests yielded statistical distributions of neck spacings and fragment sizes similar to those obtained in the experiments performed with Al6061–O rings in Zhang and Ravi-Chandar (2006) (for the same range of loading velocities), such that with increasing strain rate, more necks were nucleated at shorter distances. Janiszewski (2012) performed ring expansion experiments with cold-rolled copper Cu-ETP, Al7075, barrel steel and tungsten alloy samples with diameters varying from 27.2 mm to 33.4 mm and square cross section of 1 mm thickness. The experiments were recorded with a high-speed camera to obtain real-time observations of the necking and fragmentation processes, and to determine the expanding velocities attained in the experiments, that ranged from 85 m/s to 235 m/s. Consistent with earlier experimental data of Altynova et al. (1996), the ductility of the samples, that was estimated with a simple relation between the initial cross section area of the specimen and the cross sectional area in the uniform strain portions of the recovered fragments, was shown to increase monotonically with expanding velocity (for all materials tested with exception of Al7075). Recently, Cliche and Ravi-Chandar (2018) carried out electromagnetically driven expanding ring experiments to investigate the high strain rate behavior of AZ31B-O magnesium alloy. Some of the experiments were performed using an indirect expansion technique in which a copper pusher ring carries the electric current and launches the magnesium specimen, which remains largely free of Joule effect heating. In the remaining tests, the magnesium specimen carried the current, being heated by the Joule effect, as in the earlier tests of Altynova et al. (1996) and

Zhang and Ravi-Chandar (2006, 2008). The inner radius of the magnesium specimens was fixed at 15.75 mm, while two different thicknesses, 0.5 mm and 2.286 mm, were considered to explore the influence of the cross sectional aspect ratio of the samples in the statistics of neck development and fragmentation. The tests, that were performed for expansion velocities ranging from 50 m/s to 200 m/s, did not reveal any measurable effect of the strain rate and the Joule heating on the ductility of the magnesium samples. In contrast, the increase of the cross section size of the specimen boosted the strain developed in the unnecked regions of the ring due to the increasing time taken for the localization to develop across the thickness of the samples. Moreover, Cliche and Ravi-Chandar (2018) interpreted the experimentally observed distributions of neck spacings and fragment sizes using a simple 1D implementation of the fragmentation model of Mott (1947), and suggested that the inherent scatter in the strain to fracture of the material, which materializes in a distribution of punctual defects with low failure strain, determines the number and size of the necks and fragments formed along the circumference of the rings. The higher the strain rate of the tests, the more the distribution of defects is activated towards higher strain to failure values, explaining the increase in the number of fragments as the expansion velocity increases.

The fragmentation of metallic materials has also been investigated by means of the rapid radial expansion of cylindrical shells (Wesenberg and Sagartz, 1977; Goto et al., 2008; Hiroe et al., 2008; Zhang and Ravi-Chandar, 2010) and hemispherical shells (Mercier et al., 2010), in which the fragmentation of the samples is preceded by the formation of necking bands –in ductile materials– which are generally aligned with the direction of zero stretch (Hill, 1952; Zhang and Ravi-Chandar, 2010; Mercier et al., 2010). For instance, Wesenberg and Sagartz (1977) carried out electromagnetic expansion of Al6061–T6 cylinders 102 mm long, 127 mm in outer diameter, and 1.27 mm in thickness, at initial strain rates of $10^4\ \text{s}^{-1} \pm 5 \cdot 10^2\ \text{s}^{-1}$. The experiments were recorded using a high-speed camera, and the fragments were collected, reassembled and weighted after the tests, to determine the distribution of fragment sizes. There was a small range of preferred wavelengths, i.e. fragment sizes, into which the $6061 - \text{T6}$ cylinders fractured, in agreement with the theoretical distribution of fragments derived from the statistical theory of Mott (1947). Years later, Goto et al. (2008) explosively drove to fragmentation long cylinders fabricated from AerMet 100 alloy and AISI 1018 steel, with outer diameter of 50.8 mm, wall thickness of 3 mm and axial length of 203.2 mm, so that the loading path was close to plane strain. A part of the tests was monitored using high-speed diagnostics, including high-speed cameras, flash radiography and velocimetry of the outer surface of the specimen during expansion, and in the remaining tests soft-recovery of the fragments was performed, in order to determine the distribution of mass sizes and failure strains. The strain rate attained during the experiments was comprised between 10^4 s^{-1} and 10^5 s^{-1}, and the failure strain was found to be 0.22 ± 0.03 for AerMet 100 alloy and 0.46 ± 0.07 for AISI 1018 steel. Moreover, Hiroe et al. (2008) explosively expanded to fragmentation cylindrical metallic specimens made of 304 stainless steel, Al5052 and two different types of carbon steel. While the length of the cylinders was fixed at 100 mm, different outer diameters varying between 34 mm and 40 mm were investigated, and also various wall thicknesses ranging from 1.65 mm to 6 mm. The strain rates attained in the tests ranged between $0.5 \cdot 10^4$ s^{-1} and $5 \cdot 10^4$ s^{-1}. The experiments were recorded with a high-speed camera, and it was observed that the fractures of the cylinders generally occurred parallel to the axis. The investigation on recovered fragments revealed that the number of fragments is greater for the thinner-walled cylinders that are expanded at higher strain rates. Mercier et al. (2010) used explosive charges to expand hemispherical shells with radius of 50 mm and thickness of 3 mm, made of copper and tantalum, at strain rates of $\approx 10^4$ s^{-1}. The experiments were recorded with a high-speed camera to monitor the formation of multiple necks and the subsequent fragmentation of the specimens. The displacement of the hemispherical shells was not constrained in their equatorial plane, and thus the motion of the specimens during loading was not *perfectly spherical*, so that a small layer of the shells located near the equatorial plane was subjected to plane strain conditions, promoting early formation of multiple necking bands, parallel to each other, which eventually triggered the fragmentation of the samples. The mechanisms which control the formation of the necks were studied using a linear stability analysis and a dimensionless parameter which collects the joint effects of strain rate sensitivity, strain hardening and thermal softening of the material, so that Mercier et al. (2010) derived analytical predictions for the number of necks and the average neck spacing that were in agreement with the experimental evidence.

However, the complexity of performing fragmentation tests of rings, cylinders and hemispheres, either with explosives or with electromagnetic loading, has recently led to the development of alternative techniques to conduct fragmentation experiments using gas guns. The idea is to have *tunable* experimental setups which provide greater control over the strain rates in the specimen and extended flexibility to carry out tests in a laboratory environment, decreasing the risk for deployment of instrumentation for test monitoring. For instance, Rao et al. (2020) studied the fragmentation of metallic cylindrical shells by launching with a gas gun a polycarbonate projectile that impacts a mild steel ogive placed inside the target, making the polycarbonate projectile to flow over the ogive, thus causing radial expansion and fragmentation of the test cylinder. The cylindrical targets, made of EN3 mild steel and 304 stainless steel, were 600 mm long. Specimens with wall thickness of 2, 3 and 4 mm were tested in order to investigate the effect of specimen size and expansion velocity in the fragmentation process. The strain rates attained in the tests varied between $0.5 \cdot 10^4$ s^{-1} and $2.5 \cdot 10^4$ s^{-1}. Soft recovery of the fragments showed that decreasing the wall thickness of the cylinders increases the number of fragments, while decreasing their size and mass, and this was attributed to thinner casings being subjected to higher strain rates. Moreover, Neel et al. (2020) developed the so-called conical impact fragmentation test, a novel experimental arrangement to perform high strain rate fracture characterization of metallic materials. The setup consists of a conical specimen fired with a gas gun which is impacting a mating conical target, similar in geometry to a funnel (in the authors' words), at nominal velocities of $1 - 2$ km/s. Three tests were performed as proof of concept using specimens made of 1018 steel. Time-resolved velocity measurements obtained from the free outer surface of the conical target were used to validate simulations which revealed that, when compared with other laboratory techniques like the explosively driven cylinder expansion, the conical impact fragmentation test allows to obtain constant strain rate in the specimen and improved spatial uniformity of strain history.

In this paper, motivated by the recent works of Rao et al. (2020) and Neel et al. (2020), we have developed and demonstrated a novel fragmentation experiment which uses a light-gas gun to fire a conical projectile that impacts axially on a cylindrical tube which is expanded until multiple fractures appear along the circumference of the specimen. The impact velocities have been varied from ≈ 180 m/s to ≈ 380 m/s, leading to strain rates in the cylindrical target that range between ≈ 9000 s^{-1} and ≈ 23500 s^{-1}. We have tested additively-manufactured samples made of aluminum alloy AlSi10Mg, printed with two different qualities (*standard* and *performance*), with two different outer diameters, 12 mm and 14 mm, and two different wall thicknesses, 1 mm and 2 mm. We have characterized by X-ray tomography the porous microstructure of selected specimens before testing. Three-dimensional analysis of the tomograms has shown that the initial void volume fraction of the printed cylinders varies between 1.9% and 6.1%, and the maximum equivalent diameter of the 10 largest pores ranges from 143 µm to 216 µm, for two different printing conditions. The experiments have been recorded with two high-speed cameras to obtain time-resolved information on the nucleation and propagation of fractures. In addition, fragments ejected from the samples have been recovered, sized and weighted, so that we have obtained fragments size distributions for all tests performed. Moreover, additional X-ray tomography studies performed on recovered fragments have provided indications on the evolution of the porous microstructure in the experiments, showing that the voids deform during loading, and serve as preferential locations for the cracks propagation. To the authors' knowledge, this is the most comprehensive investigation published so far on the dynamic fragmentation behavior of additively-manufactured metals.

2. Experimental methodology

This section describes the novel high-velocity impact experiment devised to study dynamic fragmentation of additively-manufactured thin-walled tubes. The cylindrical samples were made of AlSi10Mg alloy and printed using Selective Laser Melting (SLM) technique by Materialise (2022). This material generally shows limited ductility that rarely exceeds 5% in tension (Nalli et al., 2021; Laursen et al., 2020). A key feature of the experimental methodology is that compared to dynamic fragmentation experiments in which the sample is loaded by controlled detonation of an explosive or by electromagnetic forces, the setup presented in this work is remarkable for its simplicity and rapid operation. Moreover, X-ray computed tomography scans of the porous microstructure of selected specimens were performed to determine the void volume fraction and the spatial and size distributions of voids in the thin-walled tubes. In addition, post-mortem tomograms of recovered fragments were also performed to gain insights into the influence of voids on the initiation of the fractures and the path of the cracks.

2.1. Impact testing

The experiment consists of a 25-mm bore single-stage helium-driven gun, located at the Impact Laboratory of the Carlos III University of Madrid, firing a conical-nosed cylindrical projectile that impacts axially on a tubular specimen – see an overview of the experimental setup in Figure 1. The tests were performed for impact velocities within the range 180 m/s $\lesssim v_z \lesssim$ 390 m/s, v_z being the projectile axial velocity.

The conical nosed projectile (also referred to as striker along this manuscript), machined out of a 42CrMo4 (quenched and tempered) alloy steel bar, has a spherically blunted tip to minimize aerodynamic drag and to insure a stable motion during the projectile flight. The projectile is 64 mm long, with a 1.55 mm nose radius, 40° apex angle, and a 24 mm diameter base – see Figure 2. In order to maintain the projectile centered with respect to the gun barrel, such that the projectile impacts axially on the tubular specimen, a cup-type cylindrical sabot of 24.8 mm diameter and 100 mm long, made of printed polylactide (PLA), was inserted in a 20 mm long and 10 mm diameter pin machined at the projectile base – see the indication in Figure 2. The total mass of the assembly projectile-sabot was 157 g. While the gas gun is capable of propelling a mass of 30 g up to 1 km/s, for 157 g the limit velocity is $\approx$ 400 m/s (i.e., the maximum impact velocity attained in the experimental campaign).

The impacted cylindrical samples are 40 mm long, such that one end of the specimen is mounted on a printed PLA support (hereinafter referred to as clamped end), while the other end is cantilevered (hereinafter referred to as impacted end) – see Figure 3. The PLA support is seated on a XYZ assembly formed by an XZ precision table and a height regulator jack, allowing to align the cylindrical specimen's axis with that of the gun barrel before testing. Specimens with two different outer diameters, 12 mm and 14 mm, and two different wall thicknesses, 1 mm and 2 mm, were tested. Note that the caliber of the gas gun imposes a limitation on the size of the impacted samples, as the diameter base of the striker has to be larger than the inner diameter of the cylinders in order for them to expand during the penetration process.

Upon impact, the stationary hollow cylinder is axially penetrated by the flying projectile, expanding it symmetrically until the formation and propagation of multiple cracks leads to the fragmentation of the specimen (the diameter of the cylindrical part of the projectile is approximately twice greater than the inner diameter of the cylindrical target). The nominal circumferential strain rate on the cylinder is estimated as $\dot{\varepsilon}_\theta = \frac{v_r}{r}$, where v_r is the radial expansion velocity and r is the specimen radius at half thickness. The radial expansion velocity is computed as $v_r = \frac{v_z \sin(2\alpha)}{2}$ – where the angle α is indicated in Figure 2 – under the assumption that the deforming cylinder moves perpendicular to the conical nose of the projectile, so that $\dot{\varepsilon}_\theta$ varies from ≈ 9000 s^{-1} to ≈ 23500 s^{-1} for the range of impact velocities tested. This is the same range of strain rates generally attained in electromagnetic driven expanding cylinder tests, see Section 1. Moreover, while this experiment does not show the drawback of Joule heating effects, as it is the case for cylinder expansion tests performed using electromagnetic loading, see the first paragraph of Section 1, the friction between striker and specimen may have an effect on the fragmentation process (which is difficult to assess). The impact experiments were recorded with two high-speed cameras Photron Fastcam SA-Z 2100K using a frame rate of 200 kfps for a window resolution of 256×232 px, with a shutter speed of 1/2880000 s. Two 1800-W open face lampheads were used to provide the lighting required to obtain clear-cut, high-quality images. The recordings were employed to compute the impact velocity by setting a reference length before the test and computing the time needed by the projectile to cover this length in the video footage.

In order to collect the fragments ejected from the impact, a neoprene curtain was located behind the specimen. Due to the large air flow leaving the gas gun, it was observed that most of the fragments were flying in the axial direction towards the stopping curtain, thus most of them could be recovered. Considering the soft nature of the collecting device, and given that no casing around the specimen was used, it was ensured that no further fragmentation occurred after the impact. The recovered fragments were sized and weighted, and the influence of impact velocity, specimen dimensions, and porous microstructure on the fragmentation behavior of the printed samples was studied – see Section 3.

2.2. Porosity measurements

Four samples have been investigated using X-ray tomography analysis: Alu-S-D12-t1-3, Alu-S-D12-t1-4, Alu-P-D12-t1-3 and Alu-P-D12-t1-4. The notation used for the specimens designation is as follows: Alu refers to the material (AlSi10Mg), the following letter denotes the printing quality (S refers to *standard* and P to *performance*),

Figure 1: Experimental setup for axial penetration testing of thin-walled hollow cylinders. Identification of gun barrel, high-speed cameras, lampheads, specimen support, XZ table, and height regulator jack.

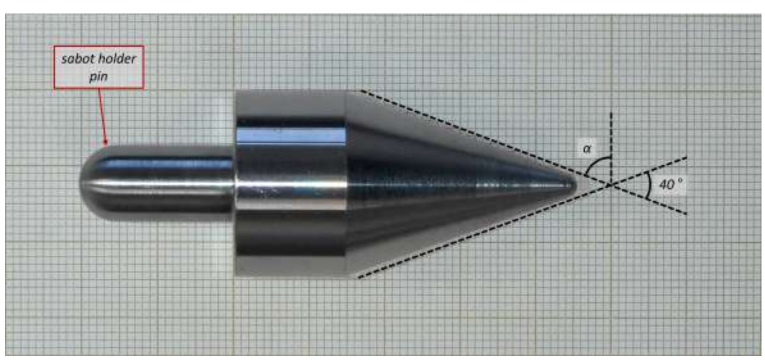

Figure 2: Cone-shaped 42CrMo4 steel projectile. Millimeter graph paper is used as a reference for the dimensions.

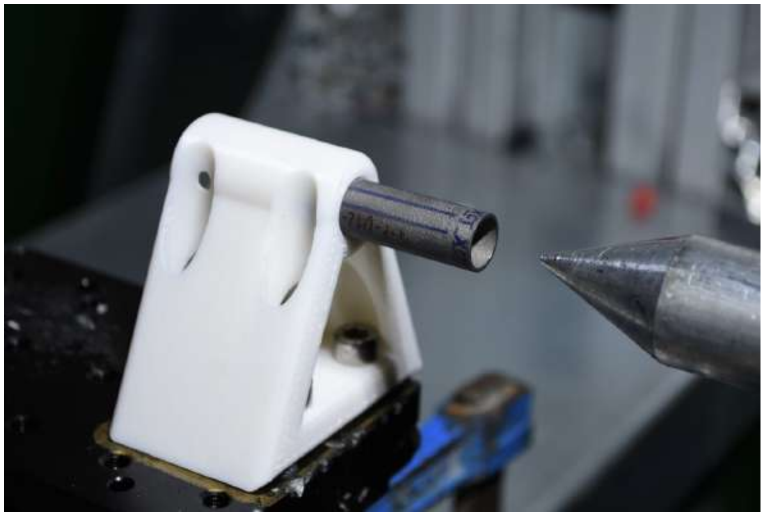

Figure 3: 3D printed AlSi10Mg hollow cylinder specimen, mounted on the PLA support before the test.

the next three alphanumeric characters indicate the outer diameter of the cylinder (12 mm or 14 mm), the following two alphanumeric characters correspond to the cylinder wall thickness (1 mm or 2 mm) and the last digit stands for the impact velocity (1, 2, 3 and 4 correspond to $\approx$ 180 m/s, $\approx$ 240 m/s, $\approx$ 320 m/s or $\approx$ 390 m/s). The complete list of the impacted samples is included in Table 2, Section 3.1.

X-ray Computed Tomography (XCT) measurements of each of the four samples were carried out in a Nanotom 160NF tomograph (General Electric-Phoenix) located at IMDEA Materials Institute. The cylindrical samples (before testing) and their fragments (after impact) were measured using 130 kV, 60 µA, and a Tungsten (W) target with 0.2 mm of Cu filter. For each tomographic inspection about 3000 radiographs were acquired for 360° rotation using 2 virtual detector mode, i.e., the detector was shifted 40° perpendicular to the beam axis to acquire 2 images that were partially overlapped to create one projection. The exposure time was set to 750 ms and 8 radiographs were averaged for each projection, leading to $\approx$ 11 hours measurement time. The source-object distance was 19 mm and the source-detector distance was 316.7 mm, yielding a 16.7 magnification with a reconstruction voxel size of $3 \times 3 \times 3$ µm^3. The reconstruction of the tomograms was carried out using an algorithm based on the filtered back-projection procedure for Feldkamp cone beam geometry (Feldkamp et al. (1984)). In addition, the analysis of the 3D reconstructed images was performed using the open source software ImageJ (Schneider et al. (2012)) and the commercial software Avizo version 2021.1 (Avizo, 2021).

The XCT measurements before testing correspond to the impacted end of the cylinders, for a total length of $\approx$ 5.4 mm, including the whole perimeter of the samples. The selected volumes enable to record sufficient number of voids to obtain statistically significant results which are representative of the actual porosity distribution in the materials. Figure 4 shows tomography images of a cross section perpendicular to the main axis of the cylinders for the four samples analyzed, obtained at a distance of 1 mm from the impacted end. The inset shows a detail of the porosity distribution in a portion of the slice. The voids appear in the form of dark spots, with a roughly circular area. For the *performance* samples, the porosity is mostly concentrated near the outer and inner surfaces of the specimens (Marvi-Mashhadi et al., 2021), having noticeably more porosity (size and number of pores) the samples printed with quality *standard*. Koutiri et al. (2018), among others, stated that the concentration of pores below the surface of SLM printed parts is caused by the inadequate connection of the hatching of the sample volume with the contour of the part. The *overall* void volume fraction for Alu-S-D12-t1-3, Alu-S-D12-t1-4, Alu-P-D12-t1-3 and Alu-P-D12-t1-4 is 6.1%, 6.1%, 1.9% and 2%, respectively (i.e., the porosity in the *performance* samples is approximately three times less). Notice that the specimens printed with the same quality have similar *overall* void volume fractions (the term *overall* is used to denote the void volume fraction of the whole specimen). In addition, note that the maximum equivalent diameter of the 10 largest pores for the *standard* samples is 216 µm, decreasing to 143 µm for the *performance* quality.

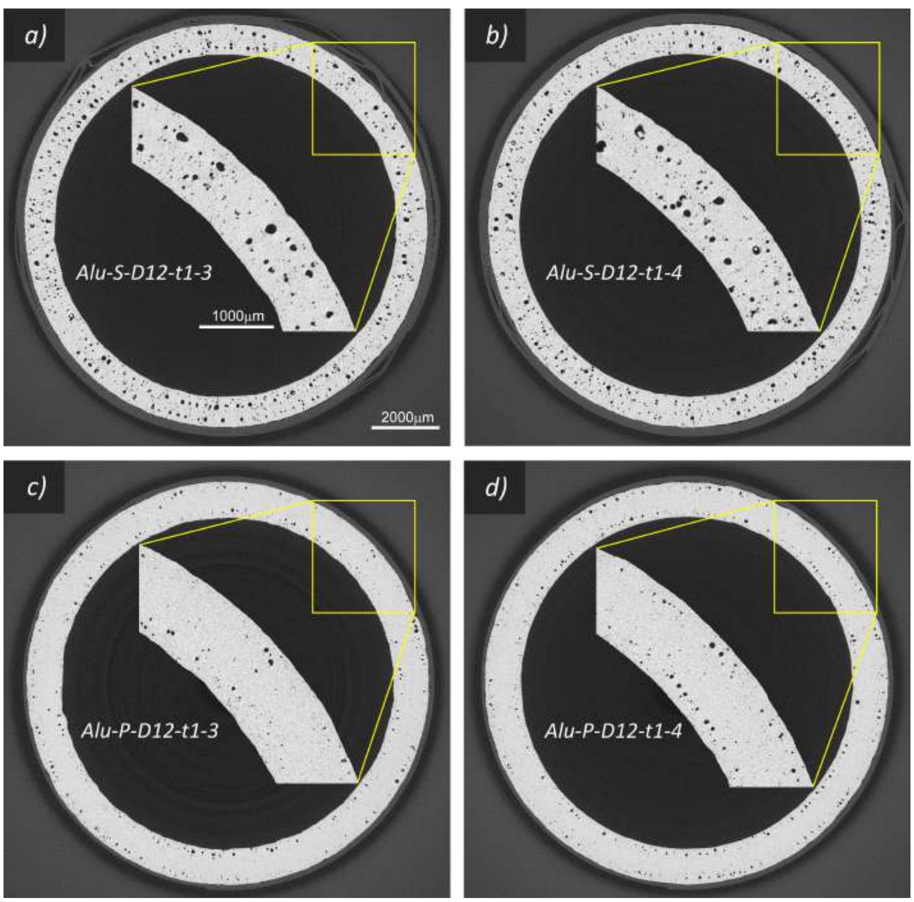

Figure 4: X-ray computed tomography images of a cross section perpendicular to the main axis of the cylinders. Results corresponding to the four samples analyzed: (a) Alu-S-D12-t1-3, (b) Alu-S-D12-t1-4, (c) Alu-P-D12-t1-3 and (d) Alu-P-D12-t1-4. All images correspond to a cross section of the tube located at approximately 1 mm from the impacted end.

Figure 5 displays 3D reconstructions of the porous microstructure showing the 3D distribution of all the pores in a portion of the scanned cylinder – see the shadowed region in Figure 5(a). The color coding of the voids corresponds with the void volume in µm^3. Figures 5(b) and 5(c) show two views of the porosity distribution in sample Alu-S-D12-t1-4. The number of large voids in this specimen is roughly homogeneously distributed in the represented sub-volume, while for its *performance* counterpart (Alu-P-D12-t1-4), the largest voids are located near the free surfaces, see Figures 5(c) and 5(d) – this is also observed in the 2D X-ray cross-section images shown in Figures 4(c) and 4(d). It is also evident the difference in void sizes of both samples: the largest void volume/diameter in the *standard* sample is almost 3/1.4 times larger than the largest void in the *performance* one. Moreover, note that the pore diameters near the outer and inner surfaces of the Alu-P-D12-t1 cylinders are up to 8 times greater than the voids in the midsection of the thickness, indicating strong gradients in the *local* void volume fraction along the thickness of the samples (i.e., the large voids near the surfaces are mainly responsible for the *overall* porosity of the *performance* cylinders). In contrast, the results presented in Figure 6 corresponding to samples Alu-S-D12-t1-3 and Alu-P-D12-t1-3 show that the *local* void volume fraction is relatively uniform along the axial and circumferential directions of the samples (the term *local* is used to denote the void volume fraction at a cross section of the specimen). The same trends have been obtained for Alu-S-D12-t1-4 and Alu-P-D12-t1-4, while the results are not shown for the sake of brevity.

A quantitative assessment of the distribution of void shapes and sizes in specimens Alu-S-D12-t1-3 and Alu-P-D12-t1-3 is shown in Figure 7. The sphericity factor S, Figure 7(a), representing the ratio of the surface area of a sphere to the surface area of the void, is computed as $S = \sqrt[3]{\frac{36\pi V^2}{A^3}}$, where V and A are the volume and the surface area of each pore, respectively. The value of S is greater than 0.9 for 70% and 78% of the voids in the samples printed with *standard* and *performance* qualities, respectively (similar results are obtained for Alu-S-D12-t1-4 and Alu-P-D12-t1-4). Assuming that the voids are spherical – which seems to be a reasonable premise attending to the computed sphericity factors – the calculation of the pore size distribution, Figure 7(b), shows that the equivalent diameter of $\approx$ 90% of the voids is less than 20 µm for both *standard* and *performance* samples (similar results are obtained for Alu-S-D12-t1-4 and Alu-P-D12-t1-4). On the other hand, note that the specimen Alu-S-D12-t1-3 contains larger pores, e.g., 4% of the voids for the *standard* specimen have an equivalent diameter greater than 50 µm, while this percentage decreases down to 1.5% in the case of the Alu-P-D12-t1-3. The corresponding mean (μ) and standard deviation (SD) for the experimental distribution of voids equivalent diameter for samples Alu-S-D12-t1-3 and Alu-P-D12-t1-3 is given in Table 1.

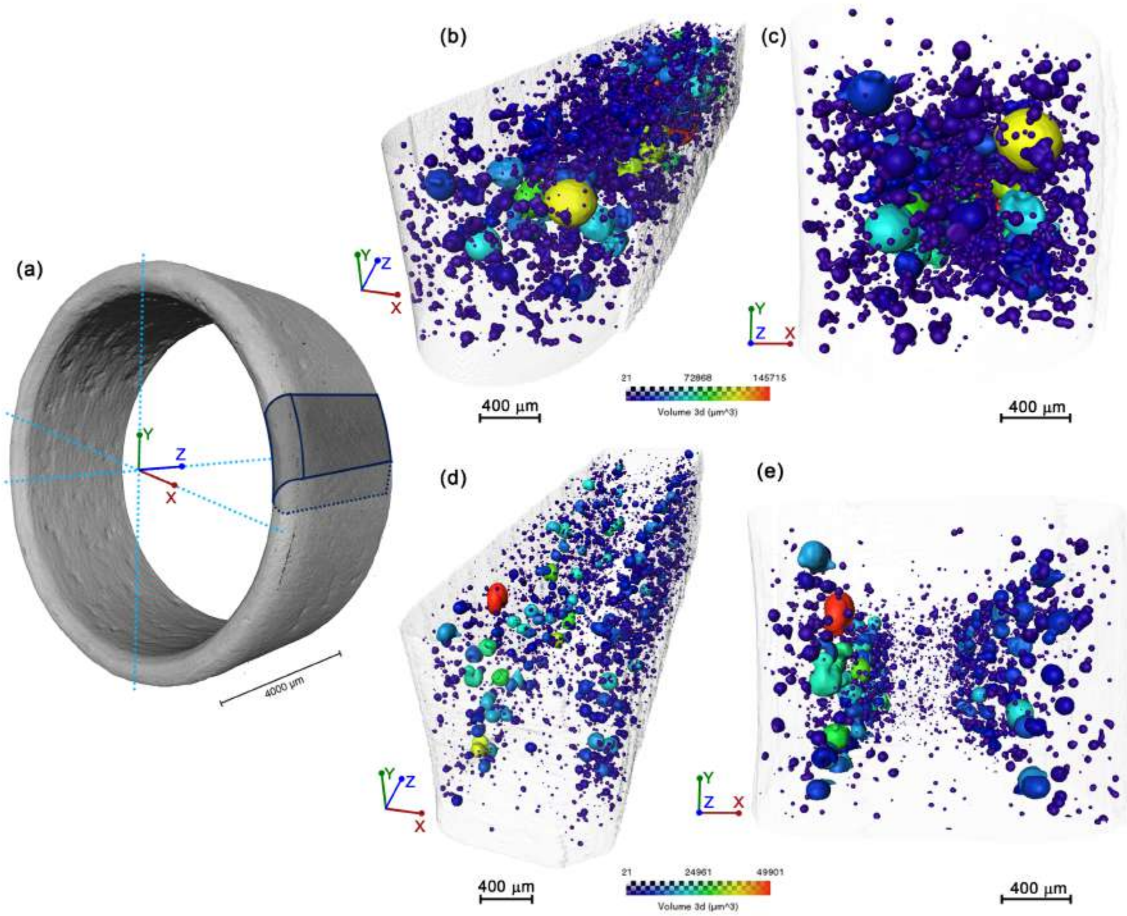

Figure 5: 3D reconstructions of X-ray computed tomography scans showing all the pores within an arbitrary portion (4.7 mm long, and ≈ 1 mm of arc distance) at the impacted end of the cylinders, corresponding to the shadowed region in (a). Results corresponding to samples: (b)-(c) Alu-S-D12-t1-4, and (c)-(d) Alu-P-D12-t1-4. For interpretation of the references to color in this figure, the reader is referred to the web version of this article.

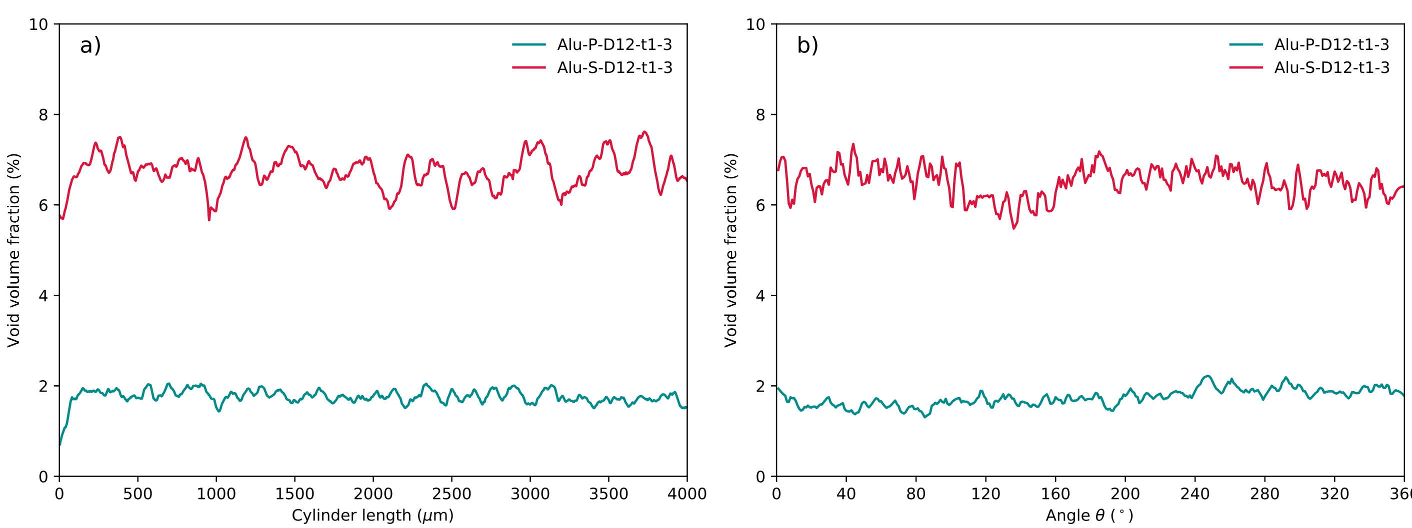

Figure 6: X-ray computed tomography data corresponding to samples Alu-S-D12-t1-3 and Alu-P-D12-t1-3. (a) Evolution of the *local* void volume fraction (%) along the axial coordinate Z. (b) Evolution of the *local* void volume fraction (%) along the circumferential coordinate Θ.

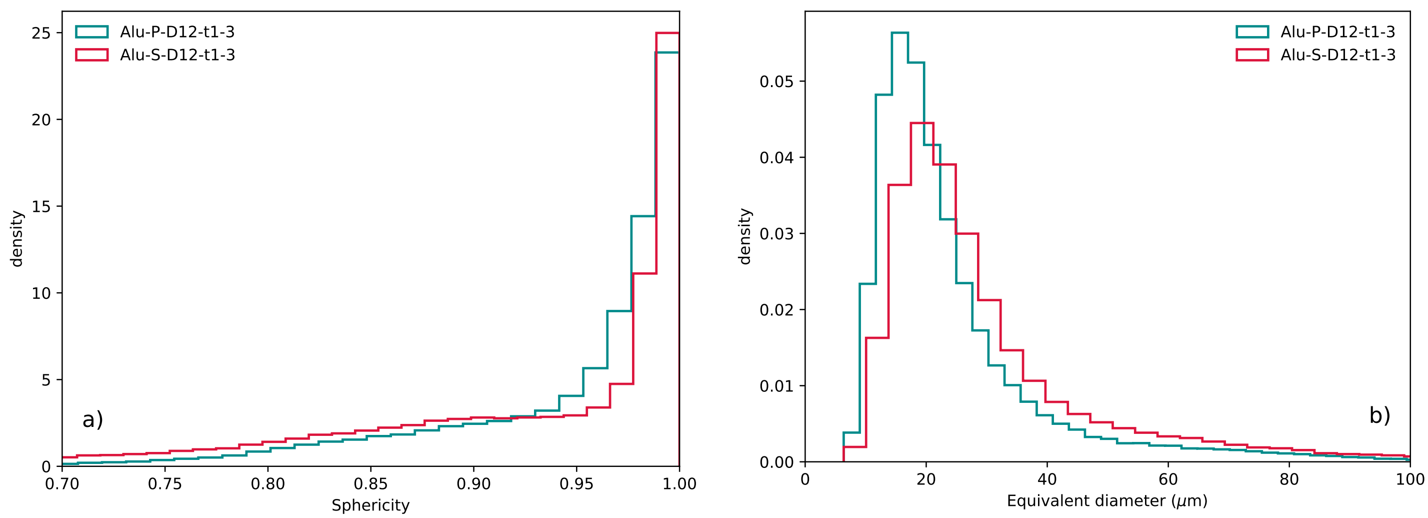

Figure 7: X-ray computed tomography data corresponding to samples Alu-S-D12-t1-3 and Alu-P-D12-t1-3. (a) Sphericity factor distribution. (b) Void equivalent diameter distribution.

Table 1: X-ray computed tomography data corresponding to samples Alu-S-D12-t1-3 and Alu-P-D12-t1-3. Mean (μ) and standard deviation (SD) of the experimental distribution of voids equivalent diameter – see Figure 7(b).

	Alu-S-D12-t1-3	Alu-P-D12-t1-3
μ (µm)	31.93	24.7
SD (µm)	22.93	15.62

The XCT measurements after testing correspond to recovered fragments, and these results will be shown in Section 3.

3. Results

This section shows the main results of the impact testing campaign, and the tomography analysis of recovered fragments. Specifically, Section 3.1 includes the summary of all fragmentation experiments, including the impact velocities, the average fragments size, and the mode of fragmentation identified from the video recordings. Section 3.1 also provides a general analysis on the mechanisms which control the formation and propagation of fractures based on the post-mortem analysis of the fragments. Moreover, the influence of impact velocity and specimen thickness on the fragmentation pattern and on the distribution of fragment sizes is investigated in Sections 3.2 and 3.3, respectively.

3.1. Salient features

The impact fragmentation campaign consists of 34 experiments. Table 2 includes specimen designation (see Section 2.2), outer diameter (D_{ext}), initial thickness (t), axial impact velocity (v_z), estimated circumferential strain rate ($\dot{\varepsilon}_\theta$), average fragment width (along the circumferential direction of the specimen) with corresponding standard deviation ($\bar{L}_\theta \pm SD$), average fragment length (along the axial direction of the specimen) with corresponding standard deviation ($\bar{L}_z \pm SD$), and description of the fragmentation pattern (a definition for *petals* and *chips* will be provided later in this section). The last four samples in Table 2 include the affix F before the last digit of designation, indicating that the outer surface of the cylinders was machined and polished after printing, as opposed to the rest of the samples that were tested as-printed. A complete summary, with separate data for each specimen, containing the width, the length, and the weight of each fragment recovered, is included in Appendix A. Note that the width and the length of each fragment was measured in three different positions with a digital caliper having a resolution of 0.01 mm, so that the mean value of the three readings corresponds to L_θ and L_z, respectively, in the sets of data of Appendix A. The average of all the values of L_θ and L_z obtained per sample gives the average fragment width $\bar{L}_\theta$ and the average fragment length $\bar{L}_z$, respectively. Moreover, note that for some of the impact experiments performed ($\approx 20\%$), the flight of the projectile slightly deviated from a straight trajectory, with the first contact between the projectile and the target occurring on one side of the tube. The specimens in which the impact deviation was greater than 0.2 mm were discarded from the present test series, i.e., they are not included in Table 2 (observe that samples Alu-S-D12-t2-4 and Alu-S-D14-t2-4 are missing here).

Table 2: The impact fragmentation campaign consists of 34 experiments, summarized as follows: specimen designation, outer diameter (D_{ext}), initial thickness (t), axial impact velocity (v_z), estimated circumferential strain rate ($\dot{\varepsilon}_\theta$), average fragment width with standard deviation ($\bar{L}_\theta \pm SD$), average fragment length with standard deviation ($\bar{L}_z \pm SD$), and description of the fragmentation pattern.

Specimen	D_{ext} (mm)	t (mm)	v_z (m/s)	$\dot{\varepsilon}_\theta$ (s^{-1})	$\bar{L}_\theta \pm SD$ (mm)		$\bar{L}_z \pm SD$ (mm)		*Pattern*
Alu-S-D12-t1-1	11.85	0.90	183.6	10777.7	5.16	0.80	16.60	6.40	chips
Alu-S-D12-t1-2	11.85	0.90	243.6	14299.8	5.10	0.41	17.29	7.55	chips
Alu-S-D12-t1-3	11.85	0.93	322.7	18995.2	5.15	0.89	12.36	7.63	chips
Alu-S-D12-t1-4	11.87	0.94	375.3	22071.2	4.85	0.78	14.24	7.63	chips
Alu-P-D12-t1-1	11.95	1.00	186.8	10965.5	5.47	1.18	11.76	4.66	petals/chips
Alu-P-D12-t1-2	12.00	1.00	246.4	14398.4	4.38	0.86	13.28	6.00	petals/chips
Alu-P-D12-t1-3	12.02	1.08	330	19389.4	4.74	0.35	10.58	2.88	petals/chips
Alu-P-D12-t1-4	12.01	1.08	387.6	22794.6	4.78	0.85	10.64	7.52	petals
Alu-S-D12-t2-1	11.90	1.90	184	11827.3	6.62	1.11	6.73	2.80	chips
Alu-S-D12-t2-2	11.85	1.90	234	15116.8	6.31	1.43	6.90	2.01	chips
Alu-S-D12-t2-3	11.85	1.90	328.5	21221.7	5.39	1.23	7.93	2.10	chips
Alu-P-D12-t2-1	12.00	2.00	193.3	12425.1	6.93	1.36	6.92	1.45	chips
Alu-P-D12-t2-2	12.00	2.00	244.9	15741.9	5.73	1.35	8.09	2.84	chips
Alu-P-D12-t2-3	12.00	2.00	325.9	20948.4	5.56	1.40	7.60	2.44	petals/chips
Alu-P-D12-t2-4	12.00	2.00	363	23333.2	5.58	1.54	10.50	3.25	petals/chips
Alu-S-D14-t1-1	13.90	0.90	187.8	9285.8	4.78	0.86	16.83	10.77	petals
Alu-S-D14-t1-2	13.90	0.90	300	14833.6	4.79	0.85	12.05	4.20	petals
Alu-S-D14-t1-3	13.90	0.95	342.8	17015.3	5.61	1.08	17.79	10.40	petals
Alu-S-D14-t1-4	13.90	0.90	386	19085.8	4.73	0.98	10.79	6.28	petals
Alu-P-D14-t1-1	14.00	1.00	191.8	9483.6	6.26	1.37	15.09	6.69	petals/chips
Alu-P-D14-t1-2	14.00	1.00	243.3	12030.0	5.10	0.71	12.61	5.44	petals
Alu-P-D14-t1-3	14.00	1.00	314	15525.8	5.31	0.85	12.74	6.80	petals
Alu-P-D14-t1-4	14.00	1.00	375	18542.0	4.81	0.95	9.75	4.82	petals
Alu-S-D14-t2-1	13.90	1.90	184.2	9866.8	7.70	1.85	6.81	1.51	chips
Alu-S-D14-t2-2	13.90	1.90	260.9	13975.3	6.38	1.93	7.36	2.43	chips
Alu-S-D14-t2-3	13.90	1.90	320	17141.0	6.08	1.76	7.80	2.52	chips
Alu-P-D14-t2-1	14.00	2.00	194.9	10439.9	9.18	2.20	9.23	2.46	chips
Alu-P-D14-t2-2	14.00	2.00	263.7	14125.3	8.63	2.83	6.98	3.17	chips
Alu-P-D14-t2-3	14.00	2.00	313	16766.0	6.57	1.54	9.66	3.23	petals/chips
Alu-P-D14-t2-4	14.00	2.00	382.4	20483.5	5.93	1.34	10.27	3.26	petals/chips
Alu-P-D14-t2-F1	13.90	1.90	198.1	10611.4	8.78	2.75	9.12	4.31	chips
Alu-P-D14-t2-F2	13.90	1.90	254.7	13643.2	6.80	1.62	10.01	3.33	chips
Alu-P-D14-t2-F3	13.90	1.90	326	17462.4	6.63	1.74	10.42	5.86	petals/chips
Alu-P-D14-t2-F4	13.90	1.90	364.5	19524.7	6.23	1.59	12.77	3.88	petals/chips

Figure 8 shows a sequence of snapshots of the impact test corresponding to specimen Alu-S-D14-t1-4. The impact velocity is 386 m/s, see Table 2. This is a representative experiment selected to illustrate the fragmentation process because of the quality of the image recording. The images on the left were taken by camera 1, while those on the right side correspond to camera 2, see Figure 1, both at equal time frame. The first pair of images – Figures 8(a) and 8(b) – shows the striker approaching the cylindrical specimen (t = −50 µs). Notice the excellent alignment of the conical nose of the projectile with the longitudinal axis of the cylinder, revealing the precision with which the experiments were performed. Figures 8(c) and 8(d) correspond to the loading time t = 0 µs, i.e., when the first contact between the projectile and the target occurs. Notice the uniform contact along the inner circumference of the tube, which is essential to ensure a homogeneous deformation along the circumferential direction of the specimen. The axial penetration of the striker leads to radial expansion and axial bending of the tube, which develops a trumpet-like shape, followed by the formation of multiple cracks at the free end of the specimen (see the white arrows in Figures 8(e) and 8(f) which correspond to t = 25 µs). No necks are observed to form in the sample before the fractures occur, most likely due to the limited ductility of this material, and due to the effect of porosity promoting early failure (see the discussion in the following paragraphs on the tomography analysis of fragments). Cracks formed at approximately the same loading time, which reinforces the idea that the striker impacts uniformly on the tube. As the projectile moves forward, and more cross sections of the cylinder get expanded, the cracks propagate along the axial direction of the tube towards the clamped end of the specimen – see Figures 8(g) and 8(h) for t = 50 µs – leading to the formation of multiple long fragments, referred to as *petals* in Table 2, which bend into an open conical shape – see Figures 8(i) and 8(j) for t = 85 µs. Note that some of the cracks get arrested, see the white arrows in Figures 8(h) and 8(i). Following the concepts of fragmentation statistics developed by Mott (1947) and Grady and Benson (1983), the arrested cracks result from the arrival of relieving stress waves from nearby fractures that remove the driving force for the cracks to progress further (see Section 1). The recovered fragments for this experiment, presenting different lengths and widths, are shown in Figure 9. During the fragmentation process some of the cracks had branched, intersected each other, or even been arrested – see for example fragments no. 13 and no. 14 marked with yellow arrows in Figures 9(a) and 9(b) (fragment numbering follows that of Appendix A). The presence of short fragments may come from long *petals* that bent until fracturing into smaller pieces.

Moreover, scanning electron microscopy (SEM) images of the fragments' fracture surface were performed using a high-resolution TESCAN MIRA-3 FEG-SEM, located at the Materials Mechanics Center of Technion – Israel Institute of Technology. Figure 10 shows three SEM fractographs at different magnifications corresponding to

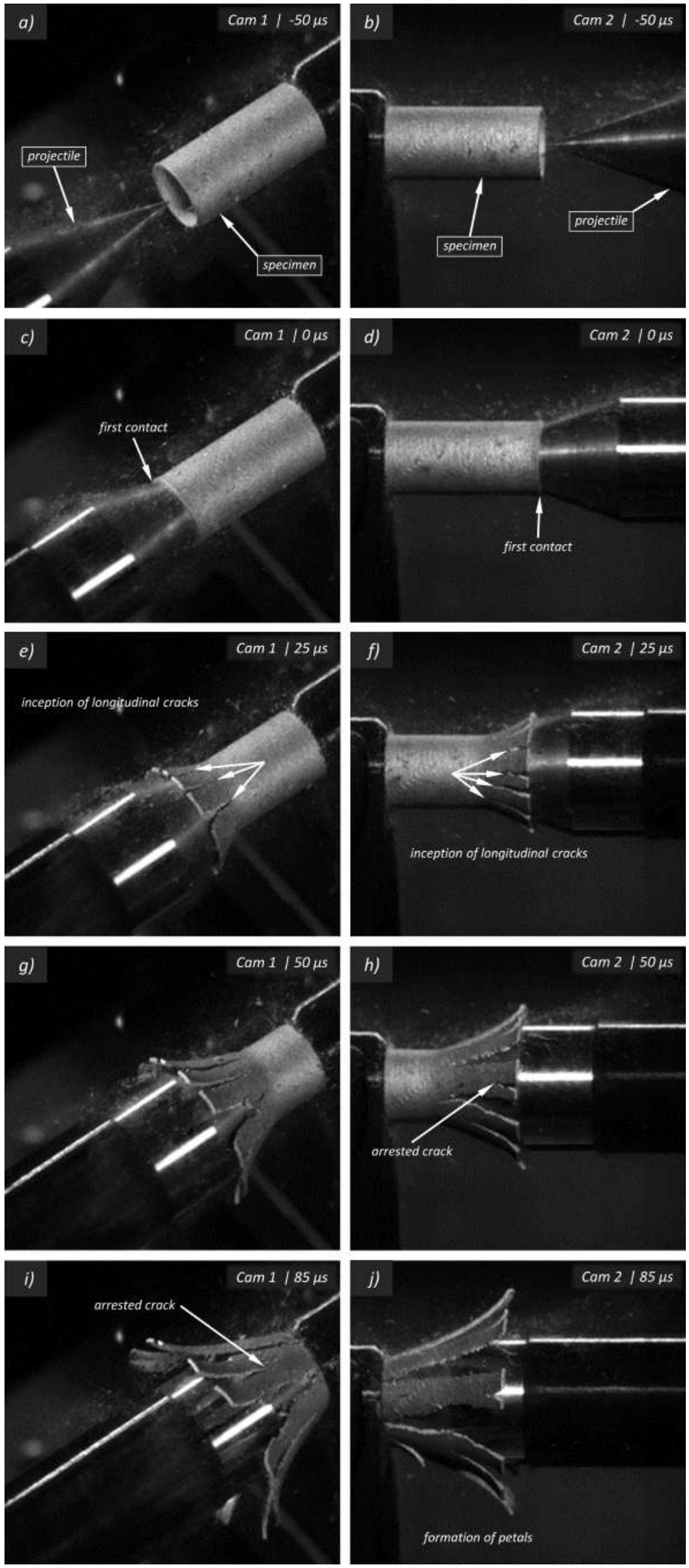

Figure 8: Image sequence of the impact test corresponding to specimen Alu-S-D14-t1-4 for different loading times: (a)-(b) t = −50 µs, (c)-(d) t = 0 µs, (e)-(f) t = 25 µs, (g)-(h) t = 50 µs and (i)-(j) t = 85 µs. The images on the left were taken by camera 1, while those on the right side correspond to camera 2. The impact velocity is $v_z = 386$ m/s.

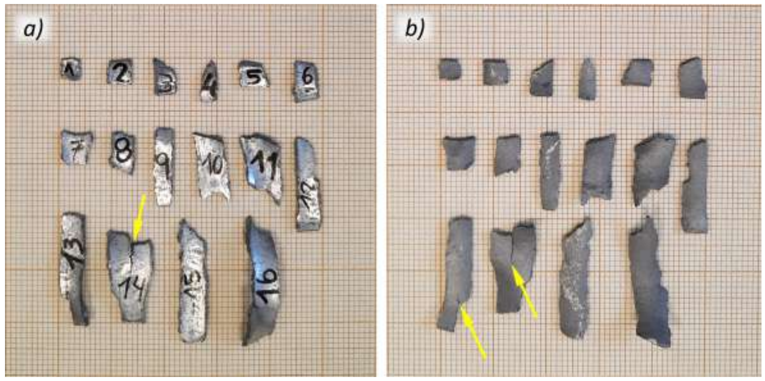

Figure 9: Post-mortem photography of the recovered fragments corresponding to specimen Alu-S-D14-t1-4: (a) inner surface, (b) outer surface. The impact velocity is $v_z = 386$ m/s. Millimeter graph paper is used as a reference for the dimensions.

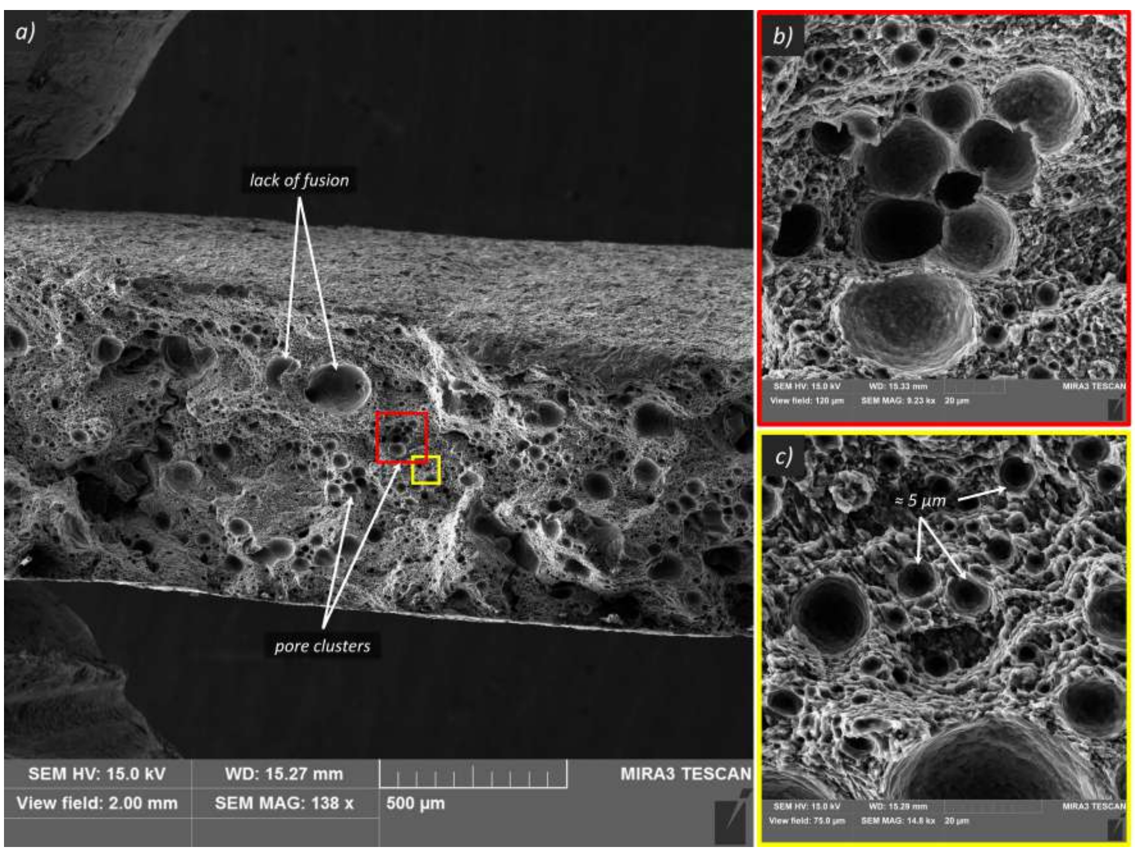

Figure 10: Scanning electron microscopy images of the fracture surface corresponding to fragment no. 12 of specimen Alu-S-D14-t1-4: (a) overview of part of the fragment fracture surface, (b) 120 µm view-field magnification corresponding to the red-squared area, (c) 75 µm view-field magnification corresponding to the yellow-squared area. For interpretation of the references to color in this figure, the reader is referred to the web version of this article.

fragment no. 12 of specimen Alu-S-D14-t1-4, in which a large amount of pores can be observed – as expected for this type of printed material. Mainly two different types of porosity were identified in the fracture surfaces: lack-of-fusion and gas porosity. While the former is usually caused by an incomplete melting during the manufacturing process (see the deep heterogeneous defects indicated with white arrows in Figure 10(a)), gas porosity is usually associated with gas trapping during particle melting (resulting in more spherical shaped pores) – note that this type of pores may be found forming clusters, with a ligament of a few microns separating them, as shown in Figure 10(b). These are common defects encountered in additive manufactured metallic materials – see Kobryn et al. (2000). The smallest void size captured by the X-ray tomography images was about 6 µm (due to the limitation on the voxel size), although the SEM fracture images reveal the presence of pores with a smaller diameter (see Figure 10(c)), suggesting that the specimens' porosity may be larger than the calculated by the X-ray analysis. Despite of the limited macroscopic ductility of the specimens, the fracture surface appearance resembles to the typical sub-micron sized elongated dimples (see the magnified fractographies in Figures 10(b) and (c)), characteristic of ductile type of failure – i.e., even though the *matrix* material may seem ductile from the microscopic perspective, ductility was shown to be low at the macroscopic level. It is unclear whether the type of fracture is intergranular/transgranular (additional microstructural analysis would be required) o simply governed by the presence of pores, although the large porosity suggests that cracks may be affected by the distribution of voids in the sample, as discussed in the following paragraphs.

Figure 11 shows a sequence of images of the impact test corresponding to specimen Alu-P-D14-t1-4. The difference with respect to the specimen shown in Figure 8 is that the sample was printed with quality *performance* (the impact velocity is only $\approx 3\%$ lower, see Table 2). The process of nucleation and propagation of cracks, and the pattern of the fragmentation, are qualitatively the same than for the *standard* specimen. The cylinder breaks into *petals*, with the average fragment width being $\bar{L}_\theta = 4.81$ mm, which is only $\approx 1.5\%$ greater than in the case of the *standard* specimen. The post-mortem photographs of the fragments corresponding to sample Alu-P-D14-t1-4 are shown in Figure 12. Likewise, SEM fractography of the fragment no. 18 of this specimen also reveals a large amount of porosity in the fracture surfaces, see Figure 13, although it presents qualitatively less lack-of-fusion defects than the specimens printed with *standard* quality (see Figure 10 for a comparison). A radial crack that started to develop (most likely due to the axial bending of the fragment) and was finally arrested can be seen in Figure 13(b). Attending at the similar fractographic characteristics, only SEM images of selected fragments of each printing quality, *standard* (Figure 10) and *performance* (Figure 13), are presented here.

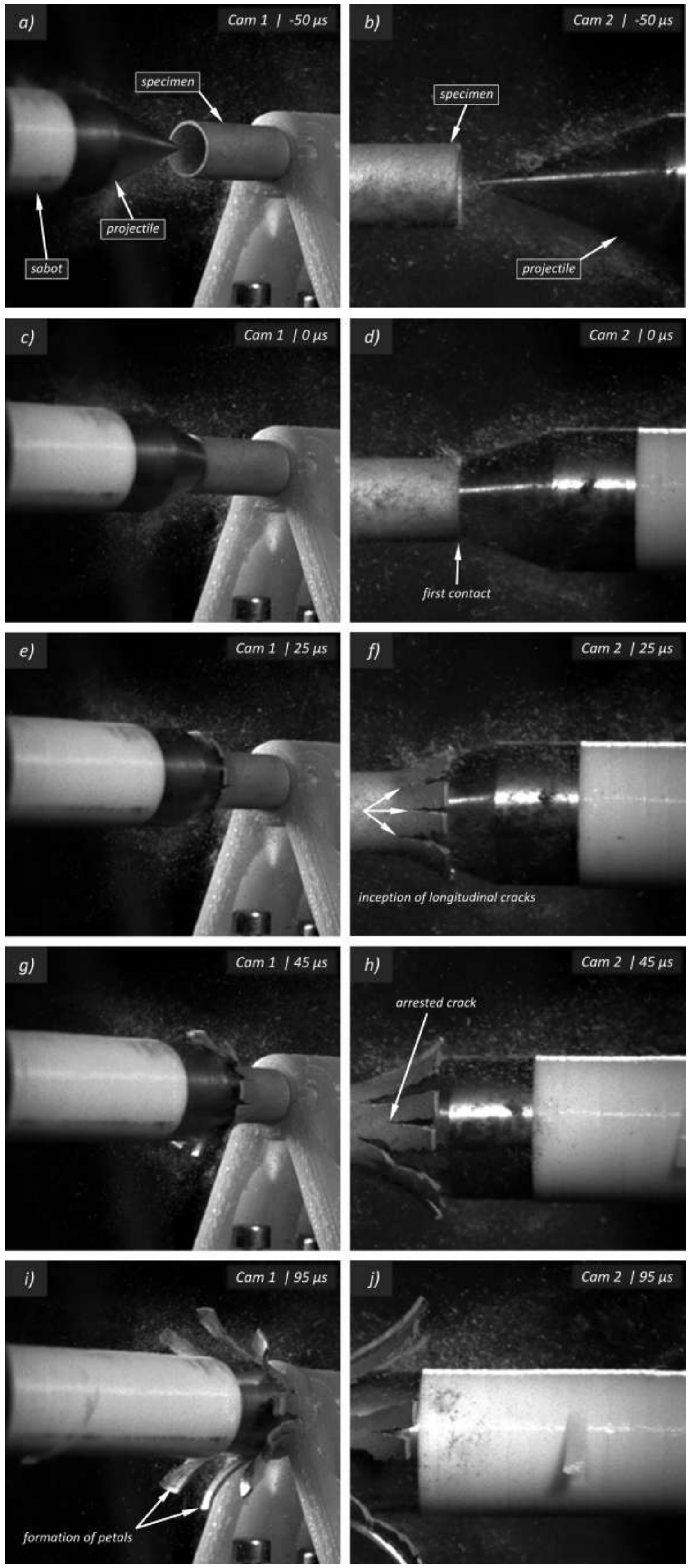

Figure 11: Image sequence of the impact test corresponding to specimen Alu-P-D14-t1-4 for different loading times: (a)-(b) t = −50 µs, (c)-(d) t = 0 µs, (e)-(f) t = 25 µs, (g)-(h) t = 45 µs and (i)-(j) t = 95 µs. The images on the left were taken by camera 1, while those on the right side correspond to camera 2. The impact velocity is $v_z = 375$ m/s.

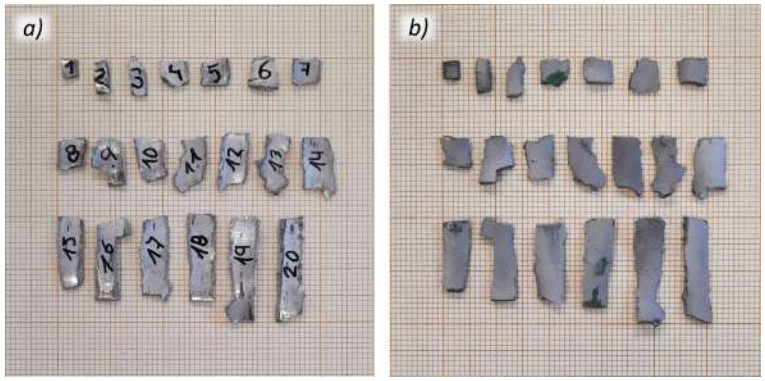

Figure 12: Post-mortem photography of the recovered fragments corresponding to specimen Alu-P-D14-t1-4: (a) inner surface, (b) outer surface. The impact velocity is $v_z = 375$ m/s. Millimeter graph paper is used as a reference for the dimensions.

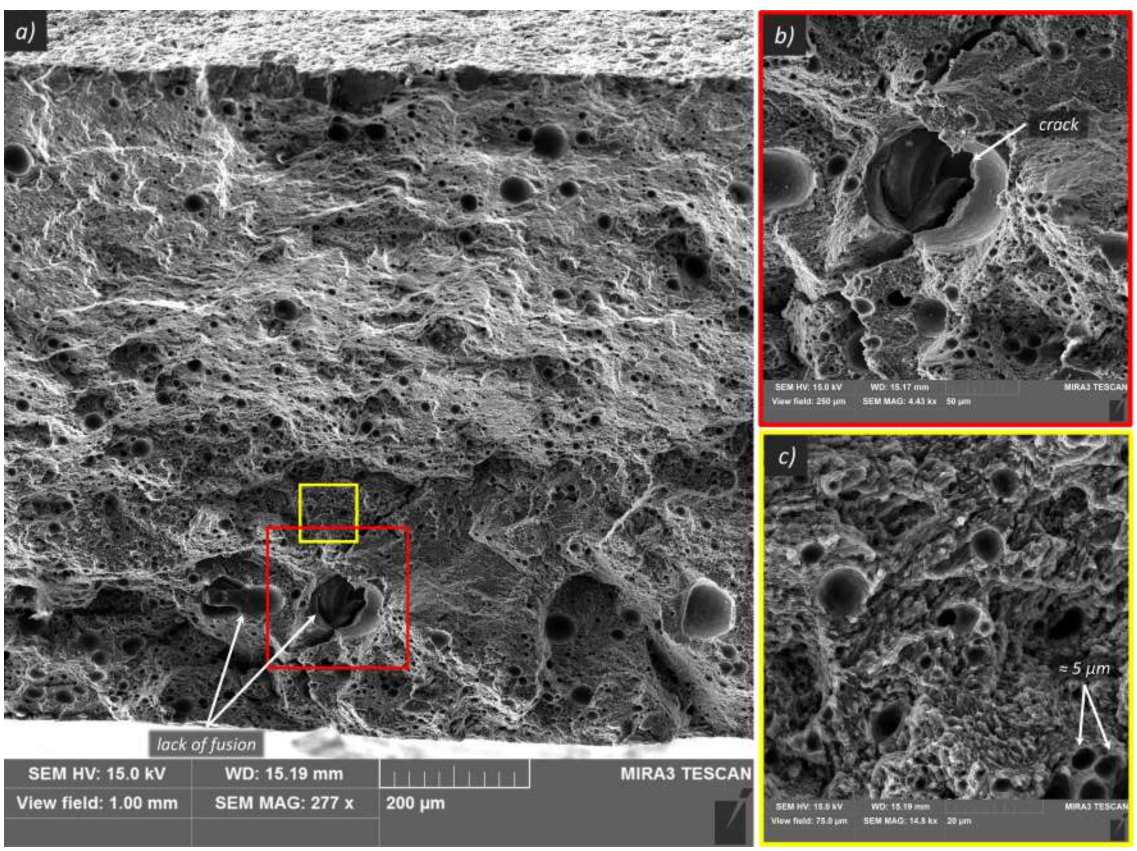

Figure 13: Scanning electron microscopy images of the fracture surface corresponding to fragment no. 18 of specimen Alu-P-D14-t1-4: (a) overview of part of the fragment fracture surface, (b) 250 µm view-field magnification corresponding to the red-squared area, (c) 75 µm view-field magnification corresponding to the yellow-squared area. For interpretation of the references to color in this figure, the reader is referred to the web version of this article.

These results suggest that, despite the differences in the initial void volume fraction, the fragmentation mechanisms and the fracture patterns for the *standard* and *performance* specimens are very similar (the same conclusions are obtained when the comparison is made for other impact velocities and sample dimensions, see Section 3.3).

The same fracture pattern, with multiple cracks propagating towards the clamped end of the specimens, and leading to multiple petals, is obtained for the four specimens subjected to pre- and post-mortem tomography analysis, see Figure 14. Note that, unlike the samples investigated in Figures 8 and 11, the outer diameter of the cylinders is 12 mm (instead of 14 mm). The impact velocities for Alu-S-D12-t1-4 and Alu-P-D12-t1-4 are 375.3 and 387.6 m/s (similar to Figures 8 and 11), while in the case of Alu-S-D12-t1-3 and Alu-P-D12-t1-3 these values drop to 322.7 and 330 m/s, respectively. Crack branching and bifurcation is noticeable in specimen Alu-P-D12-t1-3, see the white arrow in Figure 14(c).

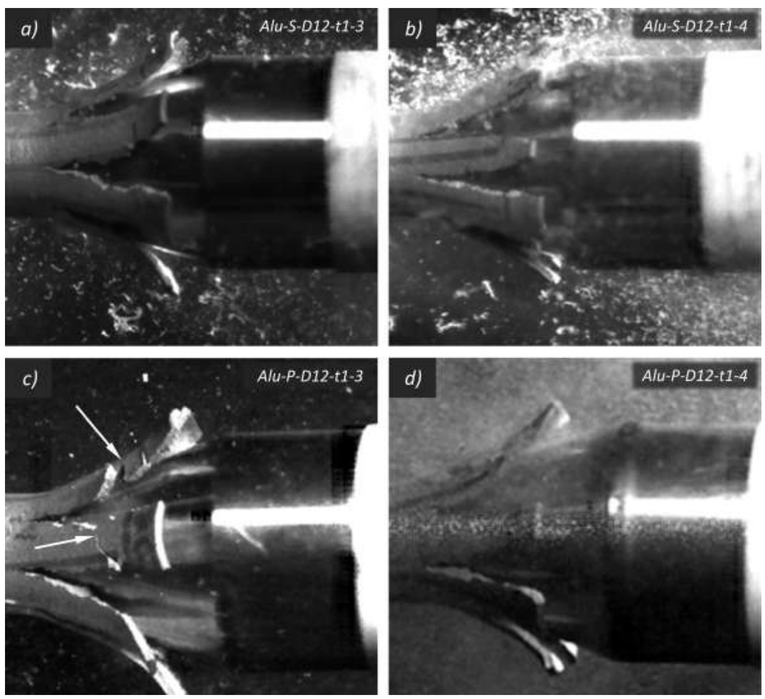

Figure 14: Snapshots showing the fragmentation patterns corresponding to the four specimens subjected to X-ray tomography measurements: (a) Alu-S-D12-t1-3 with $v_z = 322.7$ m/s, (b) Alu-S-D12-t1-4 with $v_z = 375.3$ m/s, (b) Alu-P-D12-t1-3 with $v_z = 330$ m/s and (d) Alu-P-D12-t1-4 with $v_z = 387.6$ m/s.

Moreover, the tomography analysis of the fragments provides 2D images and 3D reconstructions of the cracks leading to the fragmentation of the samples, bringing to light arrested fractures inside the fragments and providing (qualitative) information on the role of voids in the fractures path. Figure 15 shows 3D renderings of fragment no. 3 from Alu-S-D12-t1-4 specimen. Figures 15(a) and (b) show the outer and inner surface of the cylinder, respectively and at the impacted end. Multiple short cracks initiate at the outer surface of the impacted end, see the black arrows in Figure 15(a), which do not span over the specimen thickness. On the other hand, these short cracks are not observed in the inner surface, Figure 15(b). These cracks are only found in the outer surface mostly due to the larger tensile stresses occurring in the outer perimeter of the cylinder (because of the nature of the radial expansion), and the fact that the penetration of the projectile may induce compressive stresses in the inner surface. Some of these cracks propagate over a few millimeters before they get arrested in the microstructure. Figure 15(c) shows a 3D rendering of a region of the arrested crack marked in yellow in Figures 15(a) and (b). It is clear that the crack has progressed in the microstructure by linking multiple pores along the way, and its propagation is probably driven by the porosity in the material, as indicated by the large number of globular features (voids) connected to the crack surface, see Figure 15(c). The reason why these cracks did not progress further cannot be determined (unequivocally) with the post-mortem analysis of the fragments. Nevertheless, in line with the fragmentation theory of Mott (1947), it is possible that the cracks which shaped the fragment nucleated earlier (e.g., due to lower fracture strain), and their progression released the stress in neighboring sections, thus inhibiting the growth of nearby cracks (see Section 1). The fracture surface reconstruction of Figure 15(d) (as well as all surfaces inspected in different fragments) contains the footprint of the porosity, and it is interesting to note a considerable amount of large pores on the fracture surface that are probably driving the crack path. The reader is encouraged to refer back to Figures 10 and 13 to compare the SEM fractography images with the three-dimensional fracture surface renderings presented here.

To further enhance the visualization of the crack propagation in the high porosity samples (*standard* quality), Figure 16 shows two perpendicular cross sections at the locus of the crack rendered in Figure 15(c). Figures 16(a) and (c) show the X-Y plane (Z axis is parallel to the longitudinal axis of the cylindrical specimen) of the arrested crack region at ≈ 3.96 and ≈ 4.10 mm from the impacted edge, respectively. Figures 16(b) and (d) are the corresponding cross sections at the planes indicated by the red cross. These 2D tomograms show a crack that propagated in the microstructure modifying its trajectory, most likely due to the presence of large pores, trying to connect them before getting arrested, and suggesting that crack propagation is aided by the porous microstructure (at least to some extent). The same (qualitative) conclusions are valid for the arrested (either starting at the sample edge or branched from a fracture shaping the fragment) and non-arrested cracks shaping the fragments.

The comparison of pre- and post-mortem 2D cross sections for *standard* and *performance* specimens is shown Figure 17. The 3D volumes of pre- and post-mortem cylinders and fragments were correlated (also called registered) using a rigid affine transformation in 3D Slicer software (Slicer, 2022). Due to the (plastic) deformation of the

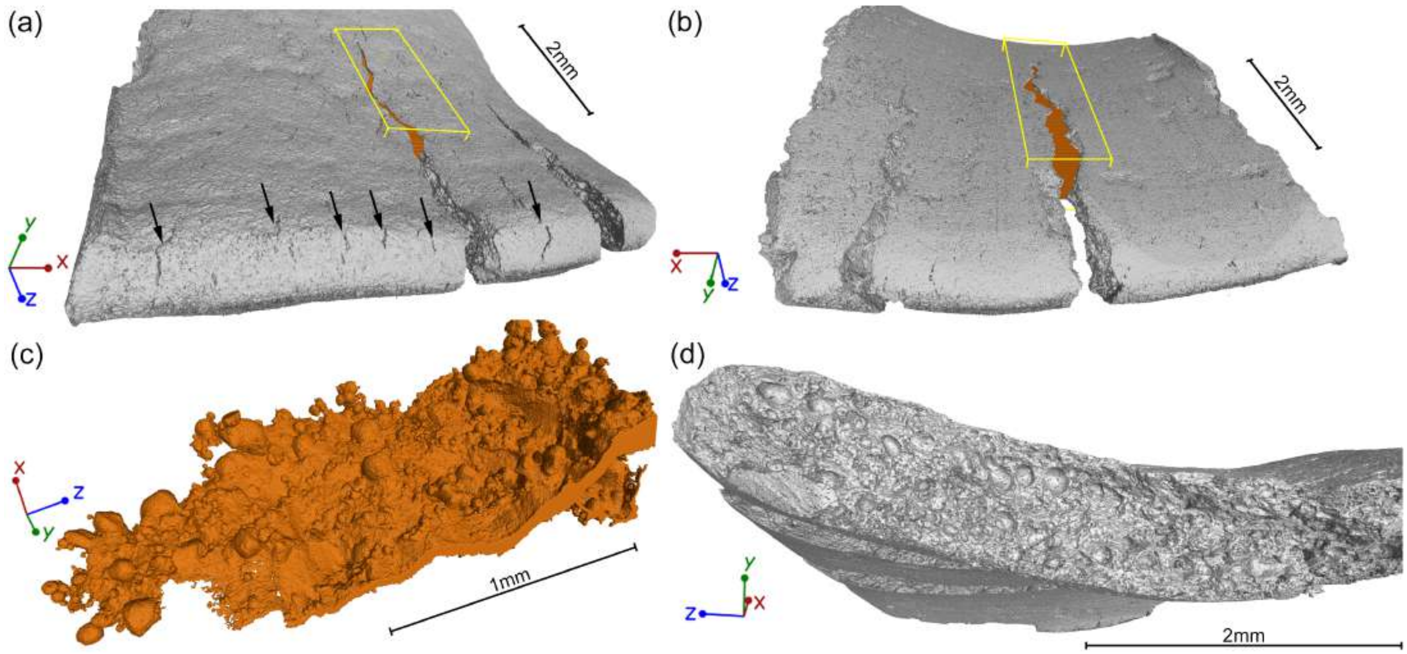

Figure 15: Fragment no. 3 of specimen Alu-S-D12-t1-4, see Table A.4: (a) 3D render of the fragment showing small cracks at the edge of the cylinder outer surface (yellow box indicates a sub-volume of an arrested crack), (b) 3D render of fragment showing the internal cylinder surface, (c) 3D render of the crack (space left in between the material) from the yellow box in *(a) and (b)*, and (d) 3D render of one of the fracture surfaces shaping the fragment showing the imprint of the pores on it.

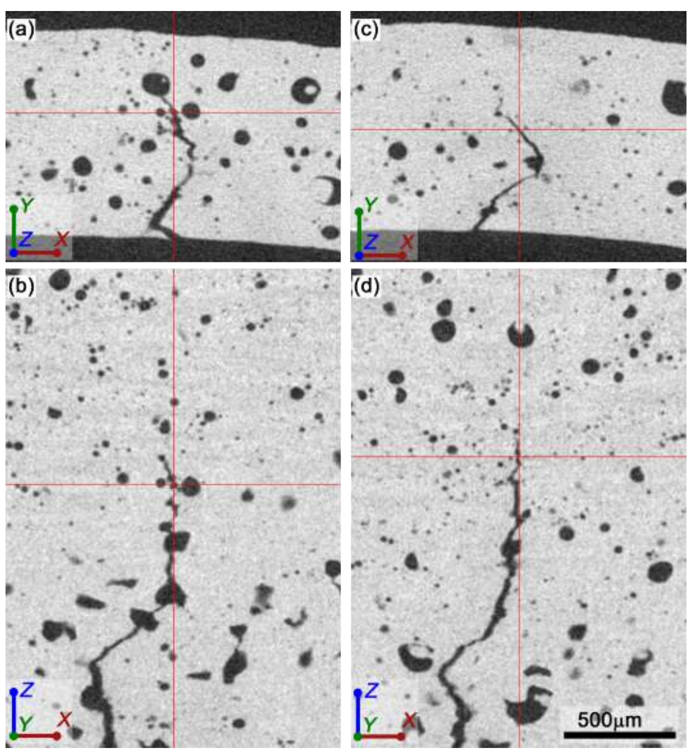

Figure 16: 2D tomograms of fragment no. 3 of specimen Alu-S-D12-t1-4, see Table A.4: (a) to (d) are perpendicular cross sections at the planes indicated by the red cross, of the arrested crack region rendered in Figure 15(c), at (a)-(b) ≈ 3.96 mm and (c)-(d) ≈ 4.10 mm from the impacted edge, respectively.

fragment with respect to the same region in the non-deformed cylinder, only a small region of the volumes was correlated. To highlight the porosity in a slab of volume, Figures 17 (a) to (c) show the projection of the minimum value of the 20 slices of (a) the undeformed sample (obtained at ≈ 4.32 mm from the edge), (b) the fragment no. 3 of Alu-S-D12-t1-4 sample, and (c) the superimposition of both *(a)* and *(b)*. The color coding presented in Figure 17(a) is such that blue defines the air (or pores), and red designates the solid material. Similarly, a gray level color table is used in Figure 17(b) (assigning dark gray to represent the air, and light gray for the material). These figures are intended to show that cracks propagate by intersecting voids, that some of them are partially elongated and distorted, indicating the development of localized plastic deformation in the vicinity of the voids, resulting from the porous microstructure. A similar methodology is used for the specimen Alu-P-D12-t1-4 and fragment no. 12, see Figures 17(d)-(f). The 3D registration was focused at ≈ 3.79 mm from the edge of the undeformed sample. To the authors' knowledge, *these are the first pre- and post-mortem X-ray tomography images ever reported showing the path of a dynamic crack in a 3D printed metallic material.*

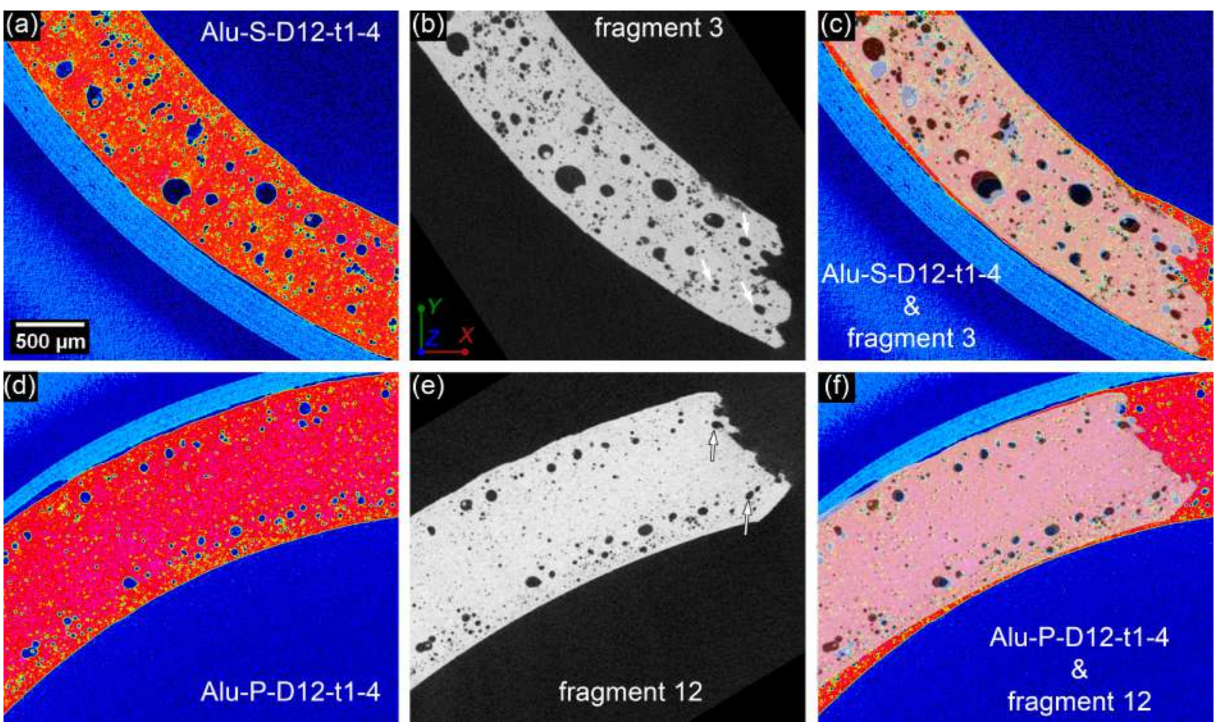

Figure 17: Comparison of pre- and post-mortem specimens for the *standard* and *performance* printing qualities: (a) section of the cylinder Alu-S-D12-t1-4 before the test, (b) portion of fragment no. 3 after impact, (c) superimposition of the same region (after correlation) of the cylinder and the fragment no. 3, (d) section of the cylinder Alu-P-D12-t1-4 before the test, (e) portion of fragment no. 12 after impact, (f) superimposition of the same region (after correlation) of the cylinder and the fragment no. 12. A projection of the minimum value of the 20 slices was performed for each sub-figure. For interpretation of the references to color in this figure, the reader is referred to the web version of this article.

Figure 18 shows a sequence of images of the impact test corresponding to specimen Alu-P-D12-t2-1. Note that the impact velocity is lower, $v_z = 193.3$ m/s, and the thickness of the specimen is double, $t = 2$ mm, than

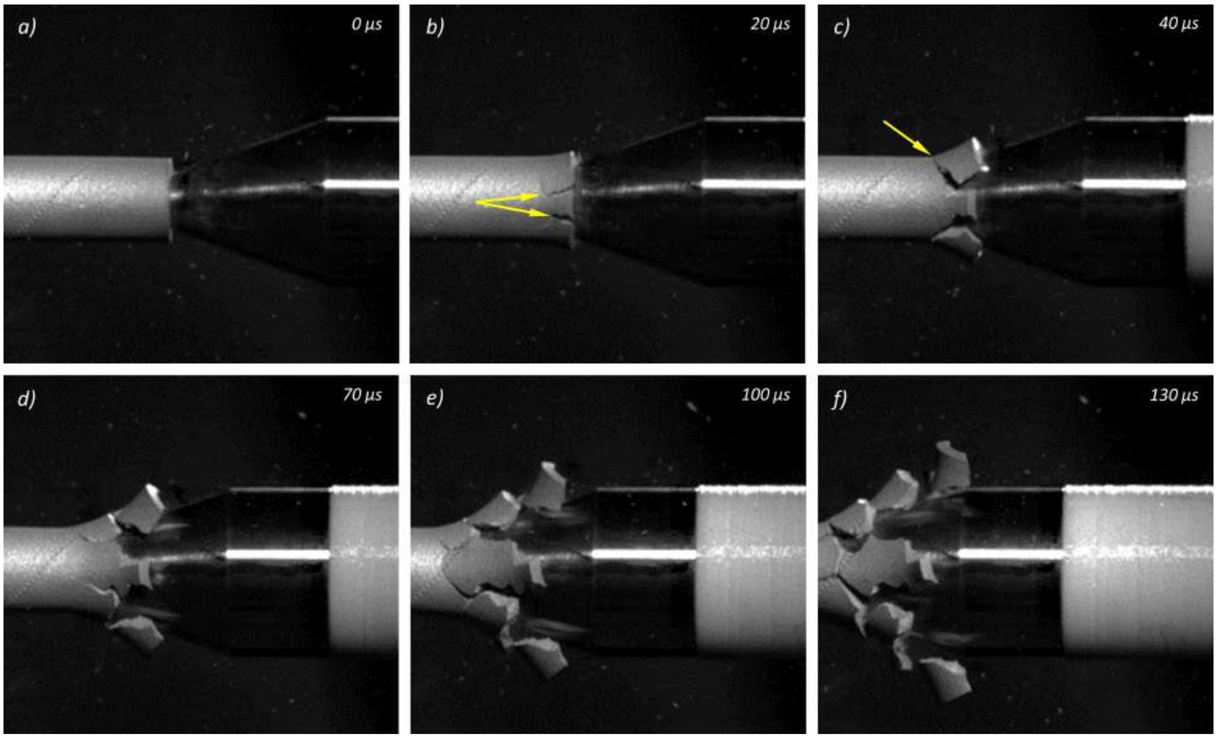

Figure 18: Image sequence of the impact test corresponding to specimen Alu-P-D12-t2-1 for different loading times: (a) t = 0 µs, (b) t = 20 µs, (c) t = 40 µs, (d) t = 70 µs, (e) t = 100 µs and (f) t = 130 µs. The impact velocity is $v_z = 193.3$ m/s.

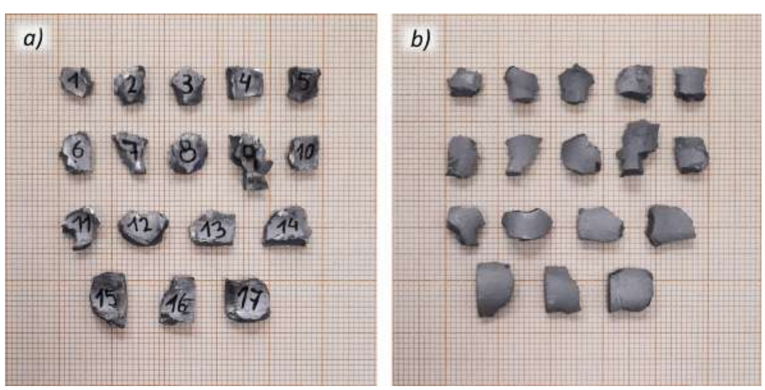

Figure 19: Post-mortem photography of the recovered fragments corresponding to specimen Alu-P-D12-t2-1: (a) inner surface, (b) outer surface. The impact velocity is $v_z = 193.3$ m/s. Millimeter graph paper is used as a reference for the dimensions.

in the tests shown in Figures 8, 11, and 14. The snapshots correspond to different loading times, starting from the first contact between striker and hollow cylinder – Figure 18(a). The onset of cracks at the impacted end is shown in Figure 18(b), see the yellow arrows pointing the fractures. Notice that the cylinder wall experiences a local axial bending as the penetration continues, as indicated by the yellow arrow in Figure 18(c). The fractures do not propagate towards the clamped end of the sample, but they zigzag intersecting each other, see Figures 18(c)-(d), leading to the formation of multiple short fragments referred to as *chips*, Figures 18(e) and (f). It seems that the local axial bending of the cylinder wall is responsible for the cracks to drastically change their trajectory, that starts following the axial direction, and twists towards the circumferential direction. Photographs of all the fragments collected for this experiments are shown in Figure 19. The average fragment width is $\bar{L}_\theta = 6.93$ mm. Note the difference with respect to the fragmentation pattern of Figures 8, 11, and 14, in which the sample broke into petals and the average fragment width was $\approx 25\%$ less. These results make apparent that both, the impact velocity and the thickness of the cylinder wall play a role in the fragmentation process, as it is further investigated in Sections 3.2 and 3.3.

3.2. The influence of impact velocity

Figure 20 shows snapshots corresponding to the impact tests of specimens Alu-P-D14-t2-F1, Alu-P-D14-t2-F2, Alu-P-D14-t2-F3 and Alu-P-D14-t2-F4, see Table 2. The samples have the same dimensions: the outer diameter and the wall thickness being 14 mm and 2 mm, respectively. They were all printed with quality *performance*, so that the only difference in the experiments is the impact velocity: 198.1 m/s, 254.7 m/s, 326 m/s and 364.5 m/s, respectively. Recall from Section 3.1 that the outer surface of these samples was machined after printing. The specimen Alu-P-D14-t2-F1 breaks into multiple *chips*, see Figure 20(a), short fragments resulting from the intersection of zigzagging cracks that start propagating axially, and suddently change their trajectory due to the axial bending of the cylinder wall, akin to the case of sample Alu-P-D12-t2-1 shown in Figure 18. The average length of the recovered fragments is $\bar{L}_z = 9.12$ mm, see Figure 21(a) and Table 2. Increasing the impact velocity up to 254.7 m/s hinders some cracks from twisting and crisscrossing, see Figure 20(b), leading to the formation of several fragments of length greater than 10 mm, raising $\bar{L}_z$ up to 10.01 mm, see Figure 21(b). For $v_z = 326$ m/s, see Figure 20(c), the chips observed for lower impact velocities have mostly turned into short *petals*, see Figure 21(c), so that the average fragment length reaches $\bar{L}_z = 10.42$ mm. Increasing further the impact velocity until 364.5 m/s, see Figure 20(d), leads to the formation of *petals* forming an open conical shape (similar to Figures 11(i) and 11(j)), raising the value of $\bar{L}_z$ up to 12.77 mm, see Figure 21(d), and making apparent the interplay between the impact velocity and the fragmentation pattern. Namely, these results suggest that the axial bending of the cylinder wall is less as the impact velocity increases, or at least it is smaller relative to the radial expansion of the tube, which is responsible for the axial trajectory of the cracks. On the other hand, note that there is not a linear relationship between $\bar{L}_z$ and v_z, and that the specific value of the average fragment length generally shows a large standard deviation, e.g., greater than the average fragment width, see Table 2.

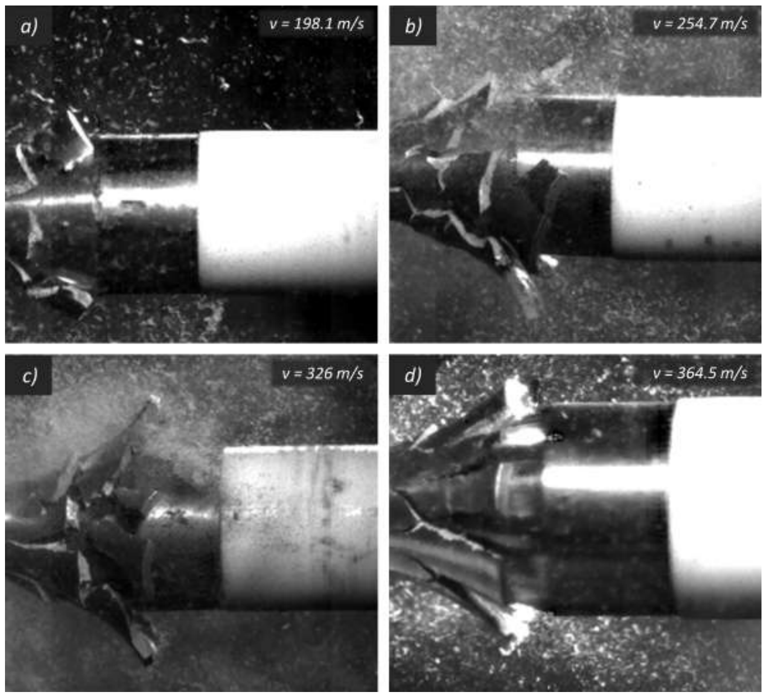

Figure 20: Snapshots showing a transition in the fragmentation pattern with impact velocity for specimens: (a) Alu-P-D14-t2-F1 with v_z = 198.1 m/s, (b) Alu-P-D14-t2-F2 with v_z = 254.7 m/s, (c) Alu-P-D14-t2-F3 with v_z = 326 m/s and (d) Alu-P-D14-t2-F4 with v_z = 364.5 m/s.

Moreover, similar observations regarding the effect of impact velocity on the length and shape of the fragments are obtained from other tests performed. For instance, Figure 22 shows that for the samples with the same dimensions and printed with the same quality, but tested in the as-printed condition (recall that the samples in Figure 20 were machined and polished after printing), the fragments also evolve from short *chips* to longer *petals* as v_z increases. It is noticeable in the snapshots of Figure 22 that there are less intersections between cracks as the striker speed increases. In addition, the average fragment length raises from 9.23 mm for an impact velocity of 194.9 m/s, up to 10.27 mm for 382.4 m/s. Moreover, Figure 23 shows snapshots of the impact tests corresponding to *performance* specimens with a smaller outer diameter, 12 mm, but keeping the same wall thickness, 2 mm. The images make apparent the transition in the fragmentation mode with the increase of the impact velocity. For the lower velocity tested, 193.3 m/s, only 5% of the fragments recovered have length greater than 10 mm, while the percentage increases up to 40% by raising the impact velocity up to 363 m/s.

Figure 21: Post-mortem photography (inner surface) of the recovered fragments corresponding to specimens: (a) Alu-P-D14-t2-F1 with $v_z = 198.1$ m/s, (b) Alu-P-D14-t2-F2 with $v_z = 254.7$ m/s, (c) Alu-P-D14-t2-F3 with $v_z = 326$ m/s and (d) Alu-P-D14-t2-F4 with $v_z = 364.5$ m/s. Millimeter graph paper is used as a reference for the dimensions.

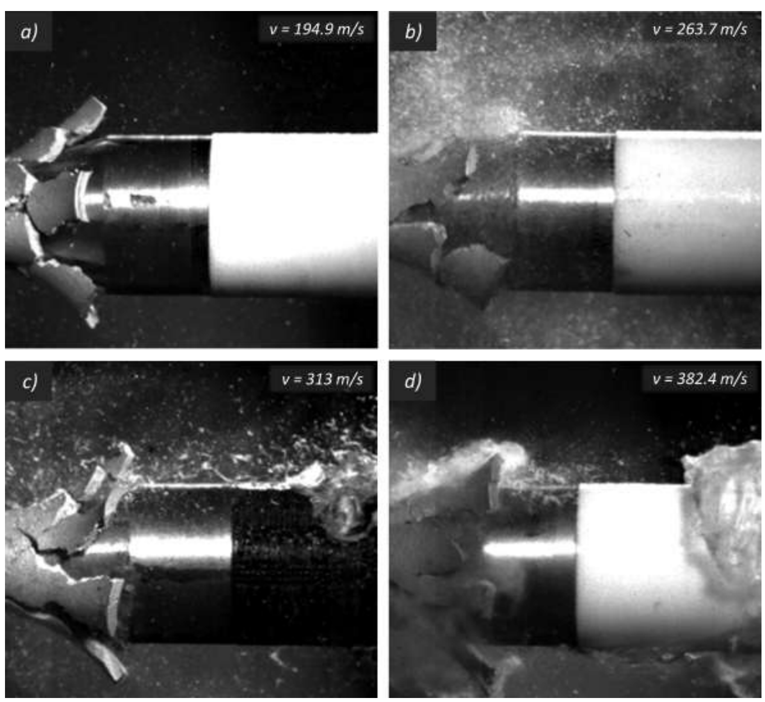

Figure 22: Snapshots showing a transition in the fragmentation pattern with impact velocity for specimens: (a) Alu-P-D14-t2-1 with $v_z = 194.9$ m/s, (b) Alu-P-D14-t2-2 with $v_z = 263.7$ m/s, (c) Alu-P-D14-t2-3 with $v_z = 313$ m/s and (d) Alu-P-D14-t2-4 with $v_z = 382.4$ m/s.

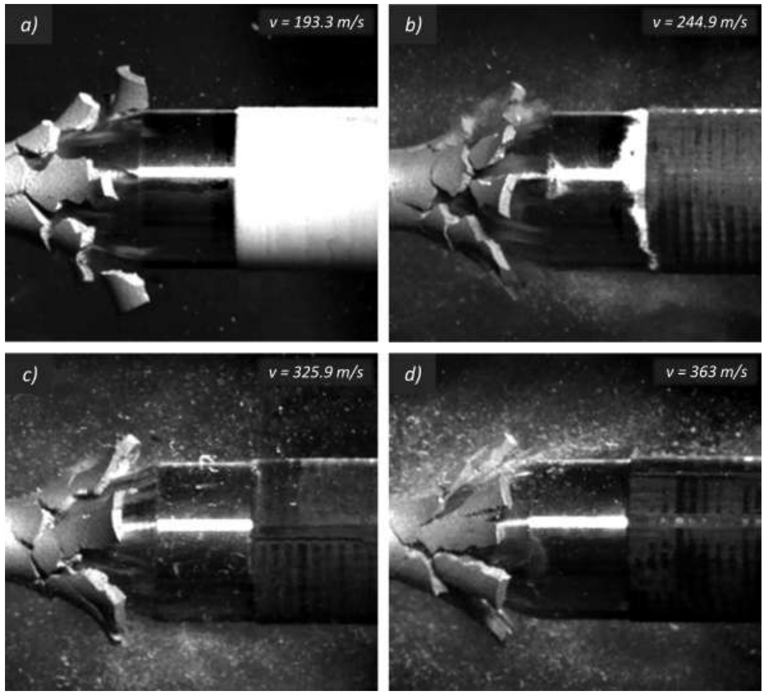

Figure 23: Snapshots showing a transition in the fragmentation pattern with impact velocity for specimens: (a) Alu-P-D12-t2-1 with $v_z = 193.3$ m/s, (b) Alu-P-D12-t2-2 with $v_z = 244.9$ m/s, (c) Alu-P-D12-t2-3 with $v_z = 325.9$ m/s and (d) Alu-P-D12-t2-4 with $v_z = 363$ m/s.

The impact velocity also affects to the width of the fragments. Figure 24 displays the distributions of fragment width L_θ as a function of the axial impact velocity, i.e, subplots (a), (b), (c) and (d) correspond to the tests performed for ≈ 180 m/s, ≈ 240 m/s, ≈ 320 m/s and ≈ 380 m/s, respectively. Note that, although the graphs include fragments recovered from both *standard* and *performance* specimens, which also have different wall thicknesses and outer diameters, they provide clear indications of the relationship between fragment width and loading rate. Namely, the range of fragment widths narrows with the increase of the impact velocity, decreasing the mean (μ) and the standard deviation (SD) of the distribution of fragments – see Table 3. The distributions of fragments have also been fitted to a log-normal probability distribution, with parameters θ (mean of the logarithmic values) and ω (standard deviation of the logarithmic values) included in the upper-right part of the subplots. It is apparent that increasing the loading speed leads to the formation of smaller fragments, showing less dispersion in width. The same trends were obtained by Zhang and Ravi-Chandar (2006, 2008) and Cliche and Ravi-Chandar (2018) for the fragmentation of rings made of Cu-101, aluminium alloys 6061–O and 1100–H14, and magnesium alloy AZ31, and subjected to dynamic radial expansion. The increasing number of fragments with the loading rate, for a metallic material with low ductility, such as the additively-manufactured aluminum alloy AlSi10Mg tested in this work, can possibly be explained relying on the statistical fragmentation theory of Mott (rather than with linear perturbation theories, which are more suitable for ductile materials that show necking localization before fracture). The idea of Mott (1947) was that, as the loading rate increases, the release waves emanating from early fractures have less time to propagate, so that the unloading does not travel quickly and far enough to inhibit further fractures at neighboring locations (see the discussion in the second paragraph of Section 1). Mott (1947) considers that the fracture sites correspond to material points with low failure strain due to the presence of defects (e.g., voids for the specimens tested in this work). Nevertheless, note that, in a real experiment, any perturbation of the loading conditions (e.g., minimal misalignment between projectile and tube for the tests performed in this work), could also have an influence on the location of the fractures that nucleate first.

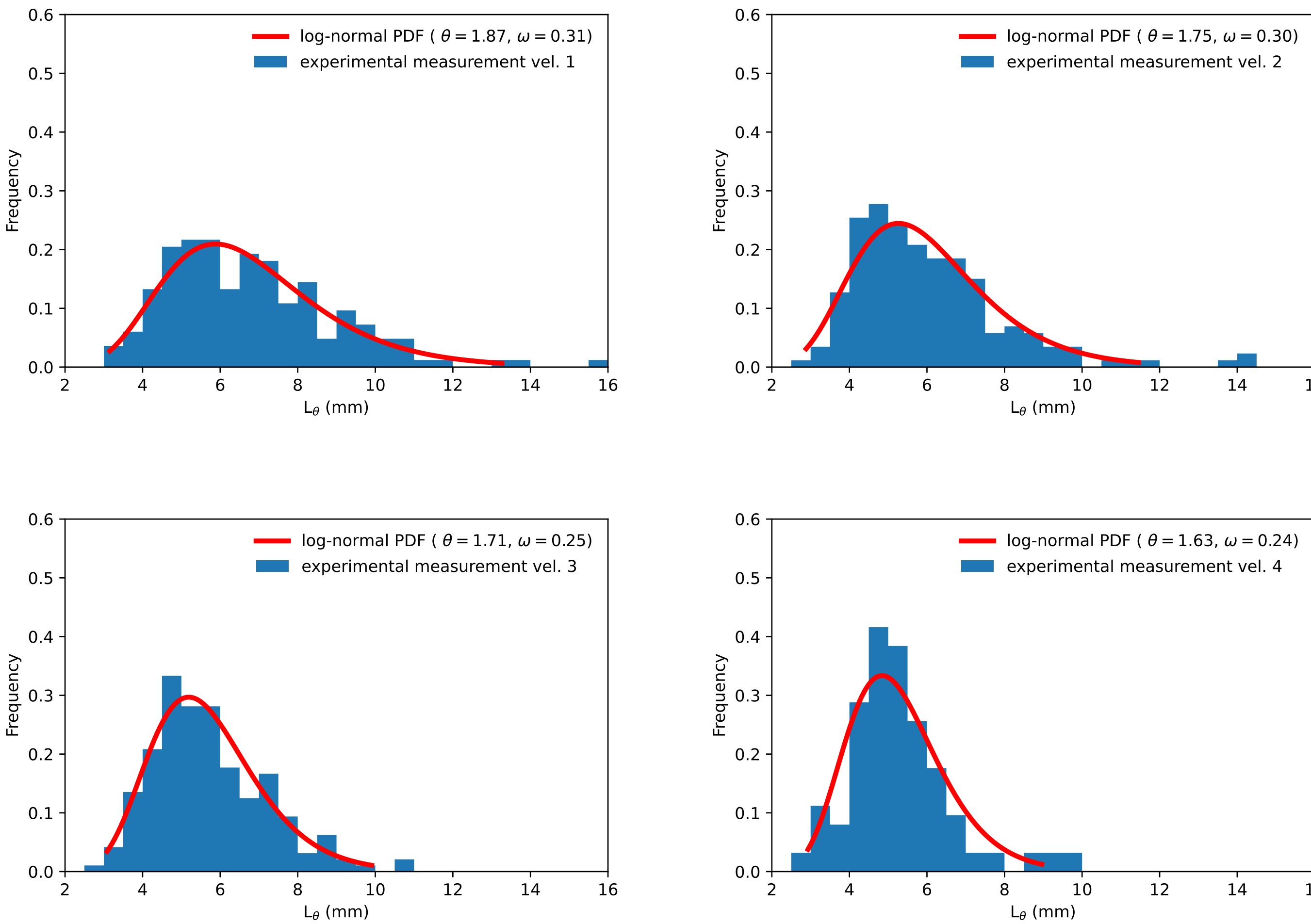

Figure 24: Distributions of fragment width L_θ including all the fragments recovered from the impact experiments, see Tables A.1-A.34. The results are collected as a function of the impact velocity: (a) vel.1 $\approx$ 180 m/s, (b) vel.2 $\approx$ 240 m/s, (c) vel.3 $\approx$ 320 m/s and (d) vel.4 $\approx$ 380 m/s. The log-normal distribution function was fitted (solid red line) to the experimental measurements of the fragments width. θ and ω are the numerical values of the lognormal distribution parameters.

The trend for the fragments to become increasingly similar in size as the impact velocity increases is further illustrated in Figure 25, which shows the average fragment width $\bar{L}_\theta$, for all the tests performed, as a function of

Table 3: Fragment width L_θ mean (μ) and standard deviation (SD) of all the fragments recovered from the impact experiments. The results are grouped as a function of the impact velocity: vel.1 $\approx$ 180 m/s, vel.2 $\approx$ 240 m/s, vel.3 $\approx$ 320 m/s, and vel.4 $\approx$ 380 m/s.

	vel.1	vel.2	vel.3	vel.4
μ (mm)	6.79	6.02	5.70	5.28
SD (mm)	2.16	1.97	1.46	1.32

the loading speed. For the lower range of impact velocities (samples tested at $\approx$ 180 m/s), the value of $\bar{L}_\theta$ varies between 4.73 mm and 9.18 mm, so that samples tested at similar loading rates provide largely different fragment sizes. However, for higher impact velocity (samples tested at $\approx$ 380 m/s), the average fragment width lies within a narrower range, 4.78 mm $\leq \bar{L}_\theta \leq$ 6.23 mm, i.e., the fragments size is less dependent on the specific sample tested, and it seems to be primarily controlled by the impact velocity (experiments at higher impact velocity are necessary to confirm this trend). Moreover, while it may be apparent in Figure 25 that the results for quality *standard* are less dispersed than for quality *performance*, a larger experimental campaign is needed to substantiate this point.

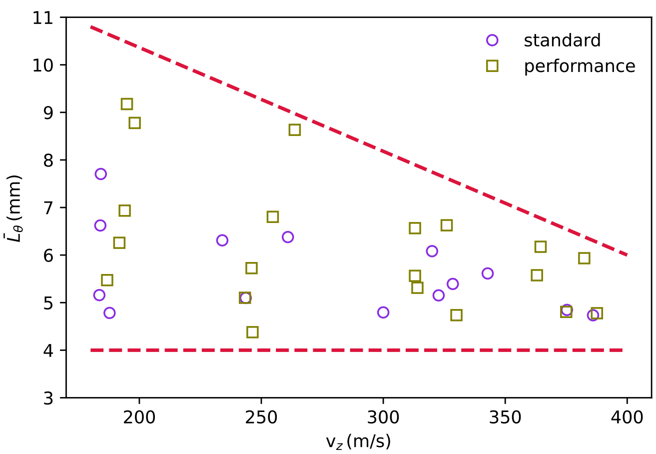

Figure 25: Variation of the average fragment width $\bar{L}_\theta$ with respect to the axial velocity v_z. Results for all experimental tests are included, see Table 2. Blue-violet circles correspond to *standard* samples, while olive squares correspond to *performance* ones. Dashed red lines are included for illustration of the experimental trend. For interpretation of the references to color in this figure, the reader is referred to the web version of this article.

3.3. The influence of specimen thickness

Figure 26 shows snapshots corresponding to the impact tests on specimens Alu-S-D12-t1-1, Alu-S-D12-t2-1, Alu-P-D12-t1-1 and Alu-P-D12-t2-1, see Table 2. The samples have outer diameter of 12 mm, and they were printed with (a)-(b) *standard* and (c)-(d) *performance* quality. All the tests correspond to the lower range of impact velocity. While the two specimens of 1 mm wall thickness, subplots (a) and (c), show a fragmentation pattern with long *petals* for which the average fragment length is 16.60 mm and 11.76 mm, respectively, the samples with 2 mm of wall thickness, subplots (b) and (d), break into multiple short *chips*, so that the corresponding values of $\bar{L}_z$ are 6.73 mm and 6.92 mm, respectively. Note that the only difference between the fragmentation patterns of *standard* and *performance* specimens is the fact that some cracks in Alu-P-D12-t1-1 tend to zigzag – see the three arrows in Figure 26(c) – without many intersections, so the cracks lead to the formation of petals with irregular shapes instead of progressing straight towards the clamped end, like in the case of Alu-S-D12-t1-1.

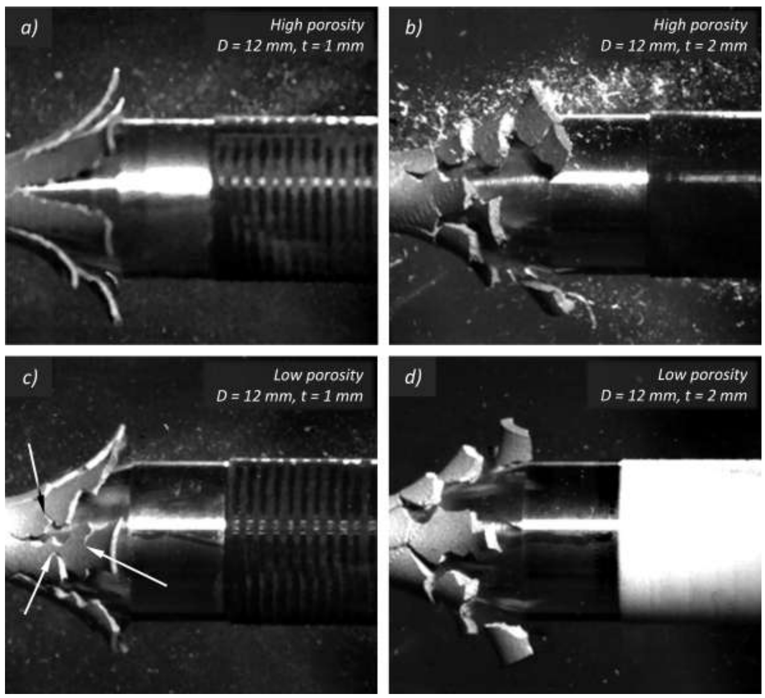

Figure 26: Snapshots showing a transition in the fragmentation pattern with wall thickness for specimens: (a) Alu-S-D12-t1-1 with $v_z = 183.6$ m/s, (b) Alu-S-D12-t2-1 with 184 m/s, (c) Alu-P-D12-t1-1 with $v_z = 186.8$ m/s and (d) Alu-P-D12-t2-1 with $v_z = 194$ m/s.

The same effect of wall thickness in the fragmentation pattern is noticed for specimens with greater outer diameter, provided that the impact velocity is within the lower range tested (the results in Section 3.2 showed that increasing the striker speed leads to the formation of petals, likewise, for the samples of 2 mm thickness). For instance, Figure 27 includes snapshots corresponding to the tests of Alu-S-D14-t1-1, Alu-S-D14-t2-1, Alu-P-D14-t1-1 and Alu-P-D14-t2-1, see Table 2. The specimens with small thickness tend to fragment into multiple long *petals*, subplots (a) and (c), while increasing the thickness to 2 mm leads to the formation of short *chips*, subplots (b) and (d). Consistent with the results shown in Section 3.2, it seems that increasing the specimen thickness raises the stresses due to the axial bending of the cylinder wall, so that the cracks that initially travel axially towards the clamped end change their trajectory, and start propagating along the circumferential direction of the

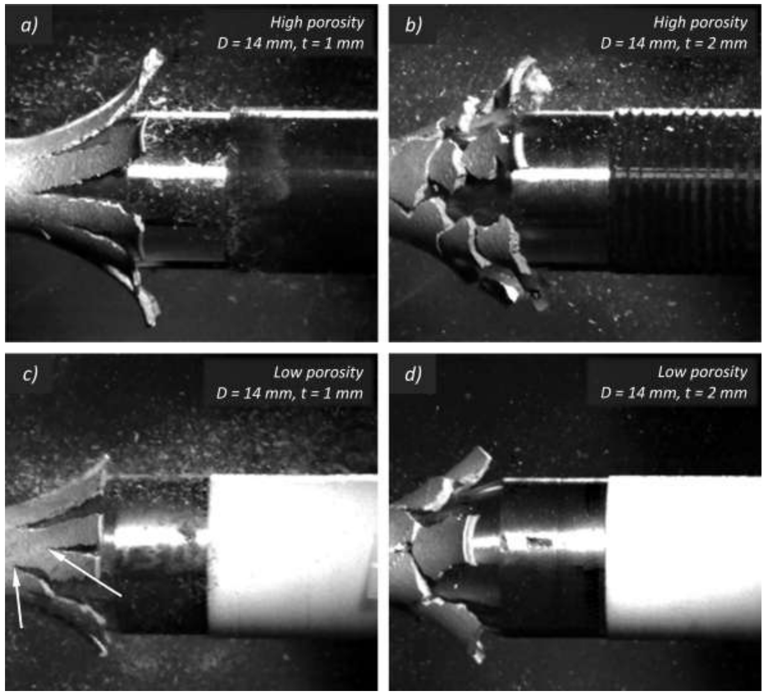

Figure 27: Snapshots showing a transition in the fragmentation pattern with wall thickness for specimens: (a) Alu-S-D14-t1-1 with v_z = 187.8 m/s, (b) Alu-S-D14-t2-1 with 184.2 m/s, (c) Alu-P-D14-t1-1 with v_z = 191.8 m/s and (d) Alu-P-D14-t2-1 with v_z = 194.9 m/s.

tube, intersecting, and giving rise to short *chips*. Moreover, notice that, in agreement with the results shown in Section 3.1 and Figure 26, there are no important differences between the fragmentation patterns in *standard* and *performance* specimens.

4. Summary and conclusions

In this work, we have presented a novel experimental setup to study dynamic fragmentation of additively-manufactured thin-walled tubes. The technique consists of a 25 mm bore single-stage helium-driven gun firing a conical nosed cylindrical projectile that impacts axially on a tubular specimen of aluminium alloy AlSi10Mg, printed by Selective Laser Melting. The thin-walled cylinder develops a trumpet-like shape as the striker moves forward, ultimately breaking into multiple fragments which have been collected, sized, and weighted. Specimens printed with *standard* and *performance* quality, with two different outer diameters, 12 mm and 14 mm, and two different wall thicknesses, 1 mm and 2 mm, have been tested at strain rates in the range from ≈ 9000 s^{-1} to ≈ 23500 s^{-1}. The experiments have been recorded with two high speed cameras, obtaining insights into the influence of specimen dimensions and impact velocity on the mechanisms of fragmentation and the pattern of fractures. Moreover, four samples were analyzed before testing using X-ray computed tomography, obtaining the initial void volume fraction, and the distribution of void shapes and sizes. Porosity has been found to be concentrated near the inner and outer surfaces of the cylinders – especially for *performance* samples – showing pores that are roughly spherical with a mean equivalent diameter of 31.9 µm for the *standard* quality, and 24.7 µm for the *performance* one, observing pores that can be as large as 143 µm and 216 µm, respectively, for the two different printing conditions. The initial void volume fraction of the cylindrical tubes printed with quality *standard* is $\approx 6.1\%$, while in the case of the *performance* samples this percentage drops to $\approx 1.9\%$. Selected recovered fragments of these four specimens were also scanned, and the computed X-ray images were employed to obtain 3D reconstructions showing the effect of the voids on the crack propagation. To the authors' knowledge, *this is the largest experimental campaign ever performed to study the fragmentation of printed metallic specimens (34 tests), and the first paper that includes 3D reconstructions of dynamic cracks in porous additively-manufactured materials.* The following list contains the main conclusions of this effort:

- As compared to dynamic fragmentation experiments in which the specimen is loaded by controlled detonation of an explosive or by electromagnetic forces, the setup presented in this paper stands out due to its simplicity and fast operation, allowing to carry out extensive experimental campaigns with relative low running cost.
- The fragmentation pattern takes the form of long *petals* or short *chips*, depending on the impact velocity and the thickness of the cylindrical specimen. For high impact velocities and thin tubes, the cracks propagate axially towards the clamped end of the sample leading to the formation of *petals*. For lower impact velocities and thicker tubes, the cracks zigzag and intersect, giving rise to the formation of *chips*.
- No necks are observed to form in the samples before the fractures occur, most likely due to the limited tensile ductility of additively-manufactured AlSi10Mg, and due to the effect of porosity promoting early material failure.
- As the ductility of AlSi10Mg is low, the multiple fracture process can possibly be explained relying on the concepts of fragmentation statistics, so that the cracks that fracture the specimen nucleate earlier at locations with low failure strain, and their progression releases the stress in neighboring sections, thus inhibiting the growth of nearby cracks, which are eventually arrested.
- Increasing the loading speed promotes the formation of smaller fragments that show less size dispersion, leading to a decrease of the mean and the standard deviation of the log-normal distribution function fitted to the experimental fragment width distributions.
- While the differences in void volume fraction between *standard* and *performance* specimens are important,

no noticeable influence of printing quality on either the fragmentation pattern or the distribution of fragment size has been observed.

- Computed X-ray tomography images of recovered fragments show that the cracks that shape the fragments include fractured voids, providing the fracture surfaces with an irregular succession of peaks and valleys, while the arrested cracks inside the fragments twist and rotate, connecting voids, following paths that seems to be laid out by the porous microstructure.
- SEM fractography analysis was performed on selected fragments, observing a large amount of pores (some of them clustered) in the fracture surfaces, arising from manufacturing defects such as lack of fusion or gas porosity. While XCT imaging could not capture voids smaller than 6 µm, SEM fractograpy revealed the presence of smaller pores. Sub-micron sized elongated dimples were also observed, as an indication of a local ductile type of failure, despite of the limited observed macroscopic ductility of the specimens.
- X-ray tomography images also revealed that voids near the cracks are elongated and distorted, indicating the development of localized plastic deformation near the voids resulting from the porous microstructure.

This work shall be extended carrying out finite element simulations of the impact experiments using the approach developed by Marvi-Mashhadi et al. (2021), thus including the actual porous microstructure of the specimens in the computational model. Such calculations, which are expected to provide additional insights into the mechanisms that control the fragmentation process, and to shed light onto the effect of the porous microstructure on dynamic crack propagation, call for modeling the flow and fracture behaviors of the matrix material, for which specific constitutive equations still need to be developed.

Acknowledgements

The assistance of Mr. Sergio Puerta and Mr. David Pedroche in the development of the experimental setup is greatly acknowledged. Likewise, thanks are due to Dr. Shmuel Ososvski for the use of the SEM at Technion, Israel Institute of Technology, to obtain the fractographic analysis, and to Prof. Daniel Rittel for the comments on the fractographies.

The research leading to these results has received funding from the European Research Council (ERC) under the European Union's Horizon 2020 research and innovation programme (Project PURPOSE), grant agreement No. 758056.

J.C. Nieto-Fuentes acknowledges support from the CONEX-Plus programme funded by Universidad Carlos III de Madrid and the European Union's Horizon 2020 research and innovation programme, under the Marie Sklodowska-Curie grant agreement No. 801538.

Appendix A. List of fragments

This section provides the width, length, thickness and weight of all fragments recovered from the impact experiments.

Table A.1: List of fragments size and mass for Alu-S-D12-t1-1.

Fragment	L_θ (mm)	L_z (mm)	t (mm)	m (g)
1	3.57	33.57	1.08	0.310
2	5.32	18.49	0.91	0.202
3	4.90	21.59	0.87	0.205
4	5.31	20.24	0.87	0.226
5	4.69	15.50	0.88	0.178
6	4.53	19.91	0.85	0.196
7	5.84	11.53	0.89	0.126
8	5.65	18.35	0.87	0.187
9	6.54	10.37	0.87	0.141
10	5.24	8.43	0.84	0.078
11	4.47	13.87	0.86	0.126
12	3.54	14.46	0.84	0.091
13	4.27	9.53	0.84	0.083
14	4.84	10.40	0.83	0.107

Table A.2: List of fragments size and mass for Alu-S-D12-t1-2.

Fragment	L_θ (mm)	L_z (mm)	t (mm)	m (g)
1	4.88	6.87	0.84	0.055
2	4.20	7.75	0.88	0.060
3	5.35	11.49	0.86	0.080
4	4.98	10.19	0.86	0.098
5	4.67	13.76	0.80	0.101
6	5.45	15.76	0.87	0.174
7	5.61	13.03	0.82	0.138
8	5.53	15.31	0.86	0.161
9	4.75	18.32	0.88	0.159
10	5.07	19.03	0.88	0.208
11	5.71	23.65	0.85	0.266
12	5.37	28.73	0.88	0.310
13	4.87	25.74	0.85	0.202
14	4.96	32.47	0.88	0.330

Table A.3: List of fragments size and mass for Alu-S-D12-t1-3.

Fragment	L_θ (mm)	L_z (mm)	t (mm)	m (g)
1	4.31	6.12	0.89	0.043
2	4.68	5.63	0.89	0.049
3	5.25	4.51	0.87	0.045
4	4.16	4.83	0.86	0.038
5	7.28	4.93	0.88	0.069
6	7.06	3.46	0.83	0.073
7	4.57	11.56	0.87	0.095
8	4.78	8.25	0.86	0.077
9	4.64	9.67	0.85	0.085
10	5.19	11.73	0.85	0.123
11	4.37	14.37	0.81	0.115
12	4.93	12.63	0.82	0.128
13	4.66	11.93	0.82	0.098
14	6.03	17.01	0.79	0.198
15	5.10	17.55	0.90	0.179
16	6.09	23.65	0.88	0.283
17	5.41	22.01	0.85	0.261
18	4.24	32.65	0.85	0.271

Table A.4: List of fragments size and mass for Alu-S-D12-t1-4.

Fragment	L_θ (mm)	L_z (mm)	t (mm)	m (g)
1	3.077	5.820	0.867	0.048
2	4.680	7.770	0.823	0.067
3	5.730	7.810	0.847	0.084
4	5.817	8.850	0.870	0.096
5	4.947	10.350	0.853	0.094
6	4.943	21.020	0.840	0.193
7	4.837	18.220	0.843	0.159
8	3.943	12.000	1.013	0.122
9	5.033	19.250	0.857	0.231
10	5.460	31.320	0.857	0.337

Table A.5: List of fragments size and mass for Alu-P-D12-t1-1.

Fragment	L_θ (mm)	L_z (mm)	t (mm)	m (g)
1	6.30	8.78	1.04	0.117
2	5.72	7.74	1.03	0.101
3	5.89	5.73	1.04	0.078
4	3.72	9.65	1.05	0.087
5	5.55	10.38	1.00	0.134
6	9.08	7.77	0.94	0.151
7	6.14	10.97	0.95	0.155
8	4.23	9.09	1.05	0.077
9	5.54	8.39	0.98	0.098
10	5.24	9.16	1.04	0.110
11	5.87	10.86	1.01	0.155
12	5.49	15.46	1.00	0.199
13	5.30	14.46	1.02	0.170
14	4.23	16.66	0.97	0.164
15	4.39	20.65	1.00	0.217
16	4.89	22.43	0.98	0.241

Table A.6: List of fragments size and mass for Alu-P-D12-t1-2.

Fragment	L_θ (mm)	L_z (mm)	t (mm)	m (g)
1	4.29	5.32	1.00	0.047
2	5.45	4.65	1.00	0.051
3	3.92	9.11	0.86	0.066
4	6.99	4.53	0.99	0.071
5	4.30	9.06	0.99	0.089
6	5.04	11.47	1.00	0.135
7	5.50	10.31	1.01	0.124
8	4.35	11.25	0.98	0.108
9	3.79	12.70	1.02	0.110
10	4.22	13.21	1.04	0.138
11	3.77	12.95	1.02	0.116
12	3.57	13.77	0.99	0.112
13	3.96	12.08	1.01	0.106
14	4.40	18.28	1.01	0.181
15	4.24	20.31	1.00	0.197
16	3.31	22.26	1.00	0.176
17	3.94	23.33	1.00	0.224
18	3.77	24.46	1.01	0.226

Table A.7: List of fragments size and mass for Alu-P-D12-t1-3.

Fragment	L_θ (mm)	L_z (mm)	t (mm)	m (g)
1	4.04	5.29	1.03	0.05
2	4.70	7.15	1.02	0.07
3	5.35	8.75	1.02	0.09
4	4.74	7.18	1.01	0.08
5	4.84	7.36	1.03	0.09
6	4.19	10.39	0.97	0.10
7	4.89	10.50	0.98	0.13
8	5.36	8.82	0.98	0.12
9	5.28	11.51	1.00	0.15
10	4.76	10.84	0.95	0.13
11	4.86	10.88	1.02	0.14
12	4.55	12.51	0.94	0.13
13	4.67	13.58	0.96	0.16
14	4.74	14.60	1.01	0.16
15	4.66	13.20	0.96	0.13
16	4.59	14.05	0.98	0.14
17	4.98	16.29	1.00	0.18
18	4.22	7.66	0.98	0.06
19	4.61	10.41	0.96	0.09

Table A.8: List of fragments size and mass for Alu-P-D12-t1-4.

Fragment	L_θ (mm)	L_z (mm)	t (mm)	m (g)
1	3.24	6.14	0.99	0.036
2	4.29	3.83	1.01	0.050
3	4.16	6.56	1.00	0.057
4	4.23	6.99	1.00	0.056
5	4.62	5.23	1.02	0.061
6	3.33	6.87	0.99	0.062
7	4.55	6.04	1.01	0.069
8	5.78	6.61	0.99	0.079
9	5.79	6.54	1.01	0.094
10	5.76	6.66	0.97	0.090
11	6.04	6.99	1.01	0.087
12	6.78	7.76	0.93	0.118
13	4.30	8.67	0.99	0.078
14	4.38	11.64	0.98	0.104
15	4.68	9.94	0.98	0.104
16	5.16	9.82	1.02	0.113
17	5.57	10.67	0.98	0.123
18	4.45	11.08	0.97	0.122
19	4.80	16.05	0.99	0.195
20	4.52	17.70	0.89	0.148
21	3.97	24.52	0.97	0.221
22	4.74	37.79	0.97	0.428

Table A.9: List of fragments size and mass for Alu-S-D12-t2-1.

Fragment	L_θ (mm)	L_z (mm)	t (mm)	m (g)
1	4.93	5.22	1.88	0.086
2	4.77	6.52	1.84	0.106
3	5.22	5.07	1.90	0.089
4	6.18	5.65	1.90	0.105
5	5.20	7.58	1.89	0.116
6	6.54	5.68	1.83	0.148
7	6.80	5.53	1.90	0.150
8	6.98	5.96	1.90	0.146
9	8.21	5.25	1.90	0.158
10	7.57	4.82	1.91	0.135
11	7.15	5.22	1.89	0.136
12	6.56	6.33	1.83	0.168
13	6.83	6.49	1.90	0.179
14	7.73	5.77	1.90	0.196
15	6.62	5.51	1.90	0.136
16	9.04	6.50	1.85	0.234
17	5.97	16.62	1.88	0.381
18	6.93	11.41	1.90	0.362

Table A.10: List of fragments size and mass for Alu-S-D12-t2-2.

Fragment	L_θ (mm)	L_z (mm)	t (mm)	m (g)
1	2.62	4.70	1.82	0.040
2	4.02	6.32	1.91	0.084
3	5.51	4.75	1.88	0.095
4	5.64	5.72	1.91	0.109
5	7.25	4.83	1.85	0.123
6	4.48	7.13	1.95	0.131
7	7.73	5.22	1.82	0.119
8	4.17	5.70	1.92	0.146
9	5.52	5.84	1.89	0.119
10	5.30	6.38	1.90	0.118
11	4.02	9.16	1.90	0.145
12	6.71	5.69	1.86	0.148
13	7.65	5.66	1.90	0.183
14	6.99	4.85	1.91	0.124
15	7.26	6.84	1.90	0.190
16	7.74	5.81	1.91	0.126
17	7.23	6.50	1.87	0.168
18	7.33	7.08	1.91	0.219
19	7.16	5.32	1.91	0.150
20	6.23	7.75	1.90	0.159
21	7.82	7.64	1.90	0.250
22	6.74	7.17	1.90	0.138
23	6.81	6.83	1.87	0.155
24	6.97	11.09	1.90	0.300
25	8.78	7.40	1.90	0.217
26	5.00	7.96	1.88	0.150
27	7.68	6.61	1.89	0.158
28	6.99	10.66	1.87	0.274
29	5.65	13.59	1.90	0.275

Table A.11: List of fragments size and mass for Alu-S-D12-t2-3.

Fragment	L_θ (mm)	L_z (mm)	t (mm)	m (g)
1	4.17	6.33	1.90	0.067
2	3.81	4.93	1.90	0.069
3	5.91	5.40	1.90	0.086
4	3.60	7.59	1.81	0.100
5	4.05	7.18	1.88	0.090
6	4.51	7.88	1.91	0.108
7	6.46	6.87	1.89	0.139
8	6.03	5.84	1.90	0.107
9	4.12	9.30	1.90	0.129
10	4.54	6.43	1.93	0.104
11	7.41	5.66	1.86	0.139
12	5.38	7.60	1.88	0.147
13	5.35	8.10	1.90	0.137
14	4.59	10.80	1.86	0.161
15	4.69	9.33	1.88	0.141
16	7.31	7.27	1.89	0.180
17	8.28	7.43	1.89	0.225
18	4.70	12.95	1.85	0.220
19	5.66	9.94	1.86	0.204
20	5.52	10.49	1.90	0.166
21	6.06	11.34	1.90	0.255
22	6.52	5.72	1.88	0.413

Table A.12: List of fragments size and mass for Alu-P-D12-t2-1.

Fragment	L_θ (mm)	L_z (mm)	t (mm)	m (g)
1	6.59	4.69	1.89	0.096
2	5.89	5.56	1.97	0.140
3	5.84	6.76	1.90	0.149
4	6.86	5.61	1.92	0.158
5	5.35	6.49	1.83	0.137
6	7.91	5.73	1.88	0.156
7	5.05	7.24	1.85	0.130
8	8.08	6.31	1.91	0.175
9	5.05	10.79	1.90	0.223
10	6.18	6.64	1.98	0.159
11	6.71	7.50	2.04	0.163
12	9.56	5.27	2.00	0.206
13	6.23	8.77	2.01	0.206
14	6.98	8.20	1.99	0.222
15	9.43	7.28	2.04	0.271
16	8.37	6.50	1.90	0.218
17	7.81	8.30	1.98	0.288

Table A.13: List of fragments size and mass for Alu-P-D12-t2-2.

Fragment	L_θ (mm)	L_z (mm)	t (mm)	m (g)
1	4.96	4.96	1.98	0.082
2	4.37	4.40	1.99	0.095
3	4.82	4.66	1.94	0.096
4	5.96	5.53	1.99	0.110
5	7.25	5.83	1.99	0.152
6	4.90	6.98	2.00	0.117
7	5.26	9.34	1.98	0.175
8	4.52	9.90	1.91	0.185
9	5.19	12.03	1.93	0.256
10	4.30	12.61	1.99	0.262
11	4.88	11.38	2.00	0.251
12	7.32	6.28	2.07	0.199
13	6.64	7.53	2.00	0.210
14	9.26	7.64	1.96	0.291
15	6.27	12.30	1.99	0.392

Table A.14: List of fragments size and mass for Alu-P-D12-t2-3.

Fragment	L_θ (mm)	L_z (mm)	t (mm)	m (g)
1	3.70	5.19	1.96	0.050
2	3.50	3.92	2.00	0.176
3	3.27	5.97	2.02	0.097
4	3.95	4.91	1.93	0.083
5	4.79	5.46	1.98	0.088
6	5.06	5.33	2.06	0.107
7	5.90	6.45	2.04	0.126
8	4.49	6.09	1.93	0.135
9	6.58	6.49	1.88	0.136
10	6.14	5.06	2.02	0.135
11	4.09	9.30	1.97	0.150
12	5.44	6.25	1.99	0.154
13	6.77	5.27	1.99	0.148
14	5.82	6.45	2.00	0.167
15	3.81	8.77	1.97	0.145
16	5.13	8.43	1.98	0.147
17	7.03	5.37	2.00	0.156
18	5.35	9.35	1.99	0.206
19	3.57	12.49	1.96	0.198
20	6.04	10.88	1.96	0.263
21	8.91	5.64	1.99	0.232
22	6.14	9.52	2.03	0.221
23	7.91	7.32	2.02	0.208
24	5.94	9.13	2.01	0.238
25	6.56	9.34	1.98	0.239
26	5.83	8.63	1.88	0.219
27	7.82	9.38	2.04	0.320
28	6.47	9.83	1.89	0.329
29	5.35	14.29	2.00	0.256

Table A.15: List of fragments size and mass for Alu-P-D12-t2-4.

Fragment	L_θ (mm)	L_z (mm)	t (mm)	m (g)
1	4.19	5.39	1.99	0.102
2	4.85	6.66	2.00	0.119
3	5.59	6.47	1.98	0.141
4	4.39	9.18	2.01	0.148
5	4.03	10.91	1.99	0.190
6	4.32	9.28	1.90	0.182
7	5.34	7.86	2.02	0.196
8	6.19	8.51	1.98	0.240
9	4.89	9.02	1.90	0.200
10	9.13	7.74	2.01	0.246
11	4.35	12.97	1.99	0.220
12	3.16	13.87	2.01	0.197
13	6.18	13.05	2.00	0.325
14	5.90	14.46	1.99	0.304
15	6.25	12.40	1.86	0.286
16	5.73	8.52	2.00	0.225
17	9.70	8.63	2.09	0.352
18	6.16	12.27	2.02	0.305
19	6.00	14.56	2.00	0.399
20	5.18	18.23	1.98	0.369

Table A.16: List of fragments size and mass for Alu-S-D14-t1-1.

Fragment	L_θ (mm)	L_z (mm)	t (mm)	m (g)
1	3.14	5.58	0.85	0.050
2	3.21	6.40	0.89	0.059
3	4.26	6.24	0.88	0.068
4	3.69	8.69	0.90	0.069
5	5.68	6.98	0.87	0.090
6	5.86	8.86	0.88	0.114
7	5.68	10.18	0.90	0.131
8	4.55	12.10	0.88	0.122
9	5.47	11.16	0.88	0.142
10	4.97	13.56	0.92	0.146
11	4.70	13.56	0.88	0.172
12	4.17	15.12	0.92	0.131
13	4.68	16.31	0.89	0.161
14	4.32	16.33	0.89	0.164
15	4.93	16.64	0.89	0.182
16	4.91	26.02	0.90	0.336
17	4.47	35.70	0.88	0.336
18	4.54	40.00	0.88	0.364
19	6.27	27.12	0.86	0.391
20	6.18	40.00	0.86	0.463

Table A.17: List of fragments size and mass for Alu-S-D14-t1-2.

Fragment	L_θ (mm)	L_z (mm)	t (mm)	m (g)
1	4.12	5.85	0.88	0.039
2	3.56	5.38	0.88	0.043
3	3.77	7.95	0.85	0.044
4	4.42	7.33	0.82	0.056
5	5.21	8.87	0.86	0.086
6	4.11	9.91	0.88	0.085
7	4.86	10.88	0.88	0.112
8	4.64	11.48	0.88	0.113
9	4.92	12.31	0.85	0.120
10	5.00	12.42	0.86	0.135
11	4.69	10.63	0.87	0.125
12	4.87	16.54	0.89	0.161
13	6.15	19.89	0.86	0.232
14	4.75	16.60	0.85	0.156
15	7.00	11.07	0.86	0.136
16	5.22	14.58	0.88	0.154
17	3.52	16.09	0.86	0.970
18	5.53	19.15	0.86	0.224

Table A.18: List of fragments size and mass for Alu-S-D14-t1-3.

Fragment	L_θ (mm)	L_z (mm)	t (mm)	m (g)
1	3.30	7.07	0.90	0.049
2	5.89	6.17	0.92	0.075
3	7.05	10.19	0.89	0.159
4	5.64	14.05	0.87	0.172
5	6.19	13.17	0.89	0.167
6	5.99	17.61	0.89	0.222
7	6.76	24.53	0.90	0.320
8	4.59	27.36	0.87	0.226
9	5.12	40.00	0.88	0.447

Table A.19: List of fragments size and mass for Alu-S-D14-t1-4.

Fragment	L_θ (mm)	L_z (mm)	t (mm)	m (g)
1	4.05	3.88	0.89	0.029
2	4.63	4.61	0.88	0.041
3	4.12	6.36	0.89	0.043
4	3.01	2.81	0.88	0.035
5	4.99	4.77	0.86	0.046
6	4.23	7.44	0.89	0.067
7	5.33	5.76	0.90	0.066
8	4.32	6.55	0.91	0.062
9	3.45	14.38	0.89	0.096
10	5.55	10.68	0.87	0.123
11	6.72	10.37	0.87	0.144
12	3.88	17.60	0.90	0.138
13	4.47	20.82	0.89	0.173
14	6.50	15.70	0.85	0.206
15	5.07	20.87	0.85	0.200
16	5.44	20.08	0.87	0.249

Table A.20: List of fragments size and mass for Alu-P-D14-t1-1.

Fragment	L_θ (mm)	L_z (mm)	t (mm)	m (g)
1	3.22	5.37	0.88	0.029
2	5.24	9.57	1.03	0.125
3	5.82	10.70	0.98	0.125
4	4.50	15.88	1.02	0.165
5	5.74	9.82	0.98	0.126
6	7.88	8.89	0.96	0.176
7	7.38	9.75	1.03	0.149
8	7.23	10.21	0.98	0.186
9	6.30	10.86	0.99	0.176
10	4.80	14.33	0.98	0.157
11	5.40	15.23	1.00	0.164
12	8.85	16.98	0.98	0.231
13	6.88	19.03	0.98	0.328
14	6.29	15.63	1.03	0.208
15	5.52	20.28	0.99	0.265
16	7.35	22.45	0.99	0.364
17	8.16	22.30	0.98	0.499
18	6.12	34.38	1.02	0.457

Table A.21: List of fragments size and mass for Alu-P-D14-t1-2.

Fragment	L_θ (mm)	L_z (mm)	t (mm)	m (g)
1	3.57	6.57	1.02	0.064
2	5.30	5.08	0.97	0.064
3	5.30	6.10	1.02	0.082
4	4.05	7.85	0.99	0.084
5	5.16	9.67	0.99	0.127
6	5.56	10.65	1.03	0.136
7	5.58	10.27	0.99	0.129
8	5.73	9.75	1.04	0.128
9	4.36	14.30	1.05	0.120
10	5.07	13.70	1.00	0.155
11	5.34	18.00	0.99	0.189
12	6.69	13.40	1.01	0.220
13	4.86	22.01	1.01	0.244
14	5.06	21.70	1.00	0.282
15	4.94	20.03	0.99	0.309

Table A.22: List of fragments size and mass for Alu-P-D14-t1-3.

Fragment	L_θ (mm)	L_z (mm)	t (mm)	m (g)
1	4.40	5.22	0.99	0.043
2	3.79	6.19	1.00	0.057
3	4.93	6.19	1.01	0.066
4	6.03	6.69	0.99	0.101
5	5.82	7.29	1.02	0.092
6	4.98	6.85	1.00	0.103
7	4.48	9.76	1.01	0.106
8	3.97	11.58	1.05	0.116
9	4.42	9.77	0.99	0.092
10	4.87	10.86	1.00	0.137
11	5.37	13.00	1.00	0.148
12	7.18	10.83	0.99	0.186
13	7.04	9.43	1.00	0.174
14	5.15	12.38	1.00	0.146
15	5.33	15.50	1.01	0.223
16	5.54	11.44	1.00	0.158
17	5.18	19.80	0.98	0.233
18	5.69	17.20	1.01	0.218
19	6.15	17.95	1.03	0.261
20	5.61	29.73	1.02	0.358
21	5.64	29.92	1.02	0.392

Table A.23: List of fragments size and mass for Alu-P-D14-t1-4.

Fragment	L_θ (mm)	L_z (mm)	t (mm)	m (g)
1	3.10	3.52	1.00	0.019
2	2.64	6.34	1.01	0.048
3	2.98	7.77	1.03	0.045
4	5.18	4.84	0.97	0.059
5	5.41	4.74	0.99	0.065
6	6.55	4.71	1.00	0.069
7	5.39	4.73	0.99	0.053
8	4.93	5.24	1.00	0.064
9	5.56	9.12	1.00	0.094
10	5.14	7.01	0.99	0.089
11	4.71	9.44	0.99	0.109
12	5.42	9.55	0.98	0.120
13	4.80	11.62	1.05	0.121
14	5.84	9.55	0.99	0.138
15	4.63	13.28	1.00	0.135
16	3.90	14.50	0.94	0.146
17	5.27	14.39	1.00	0.180
18	4.93	16.38	0.98	0.187
19	5.15	19.55	1.00	0.240
20	4.60	18.79	0.97	0.196

Table A.24: List of fragments size and mass for Alu-S-D14-t2-1.

Fragment	L_θ (mm)	L_z (mm)	t (mm)	m (g)
1	3.56	7.44	1.86	0.095
2	5.45	6.66	1.87	0.089
3	7.48	4.63	1.87	0.113
4	5.77	7.51	1.91	0.154
5	5.12	6.78	1.88	0.133
6	8.29	5.04	1.85	0.143
7	4.22	9.53	1.85	0.145
8	9.51	4.81	1.86	0.137
9	7.03	6.28	1.85	0.143
10	5.63	6.95	1.89	0.144
11	5.43	7.61	1.79	0.134
12	8.95	5.25	1.90	0.143
13	6.37	5.70	1.92	0.123
14	7.14	6.21	1.87	0.146
15	6.54	5.27	1.89	0.135
16	8.62	6.20	1.84	0.152
17	8.03	7.83	1.86	0.191
18	7.14	7.67	1.89	0.189
19	8.30	5.23	1.87	0.133
20	7.32	5.36	1.87	0.182
21	8.27	5.64	1.93	0.169
22	9.37	6.26	1.91	0.202
23	9.59	7.24	1.91	0.230
24	10.28	7.24	1.97	0.246
25	7.25	8.32	1.94	0.222
26	10.78	5.90	1.91	0.270
27	7.49	7.57	1.91	0.218
28	10.55	7.12	1.85	0.263
29	7.93	6.69	1.86	0.185
30	8.96	6.33	1.87	0.224
31	10.19	10.48	1.91	0.428
32	9.99	11.18	1.91	0.570

Table A.25: List of fragments size and mass for Alu-S-D14-t2-2.

Fragment	L_θ (mm)	L_z (mm)	t (mm)	m (g)
1	5.09	5.97	1.89	0.062
2	4.96	4.08	1.91	0.066
3	6.17	6.80	1.81	0.097
4	3.06	5.56	1.92	0.073
5	4.37	5.11	1.87	0.088
6	4.22	7.42	1.90	0.096
7	5.78	4.86	1.87	0.100
8	4.89	9.00	1.87	0.144
9	6.75	5.47	1.87	0.127
10	4.64	9.73	1.92	0.141
11	5.78	5.84	1.79	0.132
12	6.42	7.58	1.84	0.118
13	8.60	6.50	1.90	0.172
14	6.44	6.64	1.90	0.126
15	7.07	4.45	1.89	0.134
16	8.20	6.58	1.90	0.184
17	6.78	6.53	1.89	0.189
18	4.20	10.22	1.83	0.170
19	8.15	5.45	1.87	0.202
20	6.02	10.16	1.87	0.193
21	4.88	12.67	2.00	0.238
22	9.29	8.06	1.83	0.258
23	9.21	7.65	1.87	0.287
24	6.83	14.20	1.90	0.356
25	11.69	7.52	1.84	0.378

Table A.26: List of fragments size and mass for Alu-S-D14-t2-3.

Fragment	L_θ (mm)	L_z (mm)	t (mm)	m (g)
1	3.14	5.19	1.90	0.060
2	3.98	6.65	1.88	0.089
3	3.05	7.64	1.88	0.078
4	5.08	7.85	1.90	0.103
5	4.70	5.55	1.85	0.082
6	3.78	5.33	1.90	0.087
7	6.71	3.96	1.90	0.099
8	4.13	6.53	1.92	0.087
9	5.34	5.72	1.84	0.091
10	7.55	6.09	1.81	0.123
11	5.85	5.77	1.88	0.117
12	7.20	5.74	1.87	0.106
13	5.99	5.99	1.90	0.130
14	7.17	8.72	1.92	0.144
15	6.67	6.00	1.88	0.147
16	5.28	9.13	1.85	0.154
17	6.30	6.45	1.86	0.152
18	6.55	6.09	1.89	0.140
19	5.62	8.59	1.90	0.164
20	8.56	6.59	1.90	0.192
21	5.85	7.08	1.88	0.155
22	6.88	7.51	1.89	0.166
23	8.13	5.72	1.85	0.192
24	8.55	8.32	1.88	0.221
25	6.21	10.67	1.88	0.234
26	5.61	10.75	1.89	0.237
27	3.80	13.62	1.86	0.215
28	3.97	14.11	1.89	0.215
29	10.77	6.72	1.84	0.245
30	8.71	7.54	1.92	0.210
31	8.82	8.68	1.86	0.220
32	5.63	9.76	1.88	0.199
33	5.32	12.93	1.88	0.279
34	5.94	12.29	1.87	0.304

Table A.27: List of fragments size and mass for Alu-P-D14-t2-1.

Fragment	L_θ (mm)	L_z (mm)	t (mm)	m (g)
1	6.93	5.05	1.96	0.145
2	8.10	6.28	1.97	0.136
3	4.51	10.03	1.95	0.150
4	10.13	6.50	1.99	0.270
5	8.49	9.01	1.97	0.252
6	7.62	8.60	1.97	0.279
7	8.06	11.38	1.96	0.302
8	11.91	7.43	1.99	0.323
9	9.97	9.68	1.94	0.399
10	7.42	12.86	1.99	0.326
11	10.62	8.26	1.97	0.393
12	13.86	7.23	1.94	0.407
13	9.36	13.97	1.94	0.522
14	9.36	10.49	1.95	0.502
15	11.30	11.69	2.00	0.696

Table A.28: List of fragments size and mass for Alu-P-D14-t2-2.

Fragment	L_θ (mm)	L_z (mm)	t (mm)	m (g)
1	4.41	6.98	1.90	0.103
2	8.03	4.18	2.01	0.148
3	8.81	8.00	2.02	0.185
4	6.23	8.30	1.94	0.190
5	8.49	7.75	2.00	0.230
6	9.53	8.81	1.90	0.234
7	8.13	8.64	2.01	0.230
8	8.71	6.90	2.00	0.223
9	6.19	9.87	1.99	0.221
10	5.78	12.67	1.99	0.282
11	6.57	10.46	2.02	0.298
12	6.59	15.91	1.99	0.370
13	8.19	11.82	2.05	0.439
14	11.00	10.03	2.25	0.511
15	14.11	8.76	1.96	0.509
16	5.99	18.15	1.97	0.486
17	8.94	12.79	1.98	0.526
18	13.96	9.18	1.99	0.504
19	14.38	8.45	1.96	0.564

Table A.29: List of fragments size and mass for Alu-P-D14-t2-3.

Fragment	L_θ (mm)	L_z (mm)	t (mm)	m (g)
1	2.71	8.29	1.97	0.096
2	6.81	5.95	2.00	0.121
3	6.92	3.92	2.01	0.107
4	6.05	7.02	1.98	0.132
5	4.46	7.95	2.00	0.154
6	7.79	7.23	1.95	0.161
7	5.38	9.21	2.01	0.172
8	7.88	7.97	1.98	0.208
9	5.69	7.64	1.95	0.171
10	4.88	9.06	1.96	0.168
11	7.42	7.18	2.00	0.192
12	5.35	5.93	2.01	0.194
13	7.23	10.90	1.98	0.263
14	7.22	10.66	1.92	0.284
15	9.25	8.34	1.91	0.260
16	5.32	14.72	1.96	0.313
17	5.66	12.66	1.99	0.359
18	8.10	10.64	2.06	0.388
19	6.15	16.67	1.99	0.434
20	7.71	11.47	1.86	0.355
21	7.58	11.21	1.99	0.391
22	9.54	10.75	2.01	0.448
23	5.94	16.98	2.01	0.430

Table A.30: List of fragments size and mass for Alu-P-D14-t2-4.

Fragment	L_θ (mm)	L_z (mm)	t (mm)	m (g)
1	4.91	6.16	1.98	0.098
2	7.78	5.46	1.92	0.122
3	4.90	8.27	1.94	0.158
4	4.14	10.25	1.95	0.173
5	5.19	6.21	1.99	0.205
6	8.66	7.01	1.91	0.225
7	6.16	9.74	1.91	0.207
8	7.47	9.30	1.85	0.204
9	5.43	11.52	1.99	0.199
10	6.44	7.19	1.97	0.172
11	6.69	7.81	1.89	0.233
12	5.65	9.08	1.94	0.226
13	5.20	10.80	1.89	0.260
14	4.92	11.28	1.95	0.254
15	5.72	11.35	2.01	0.260
16	9.17	8.38	2.00	0.233
17	5.13	13.54	2.00	0.248
18	6.16	13.49	1.98	0.283
19	4.88	10.60	1.98	0.240
20	5.72	12.38	1.81	0.309
21	7.38	10.78	1.96	0.321
22	4.20	15.83	1.92	0.288
23	4.59	19.81	1.96	0.402

Table A.32: List of fragments size and mass for Alu-P-D14-t2-F2.

Fragment	L_θ (mm)	L_z (mm)	t (mm)	m (g)
1	3.31	8.55	1.93	0.092
2	5.31	5.54	1.86	0.110
3	6.33	8.22	1.92	0.162
4	5.47	12.68	1.90	0.231
5	7.06	7.46	1.91	0.215
6	6.84	7.39	1.89	0.175
7	6.11	8.96	1.93	0.196
8	6.45	8.84	1.87	0.266
9	6.42	7.01	1.95	0.214
10	5.60	12.15	1.92	0.246
11	6.08	10.60	1.87	0.258
12	6.16	7.48	1.81	0.192
13	9.55	7.12	1.82	0.236
14	7.14	11.35	1.87	0.336
15	7.45	13.76	1.89	0.392
16	7.48	13.30	1.89	0.371
17	6.51	11.01	1.82	0.345
18	9.82	9.10	1.87	0.373
19	10.64	9.01	1.84	0.441
20	6.34	20.75	1.87	0.553

Table A.31: List of fragments size and mass for Alu-P-D14-t2-F1.

Fragment	L_θ (mm)	L_z (mm)	t (mm)	m (g)
1	5.08	4.94	1.70	0.081
2	4.35	7.08	1.86	0.132
3	9.84	5.67	1.86	0.174
4	7.48	6.32	1.93	0.188
5	7.14	7.79	1.83	0.146
6	6.84	7.11	1.84	0.176
7	8.38	7.22	1.91	0.234
8	7.07	9.24	1.87	0.287
9	10.70	7.25	1.89	0.288
10	9.34	9.60	1.86	0.319
11	7.92	12.14	1.92	0.353
12	9.32	9.08	1.88	0.375
13	10.14	8.64	1.91	0.361
14	7.85	24.25	1.87	0.710
15	15.55	8.47	1.84	0.540
16	13.46	11.18	1.91	0.753

Table A.33: List of fragments size and mass for Alu-P-D14-t2-F3.

Fragment	L_θ (mm)	L_z (mm)	t (mm)	m (g)
1	4.29	9.36	1.81	0.131
2	5.15	5.69	1.92	0.107
3	4.43	6.14	1.94	0.119
4	4.34	8.77	1.88	0.127
5	7.32	6.87	1.90	0.168
6	7.23	8.53	1.81	0.169
7	8.50	6.81	1.88	0.174
8	7.34	7.44	1.84	0.175
9	6.27	8.61	1.90	0.210
10	4.86	11.29	1.88	0.243
11	7.90	11.64	1.88	0.258
12	6.67	11.95	1.94	0.277
13	9.01	8.34	1.84	0.258
14	5.55	13.05	1.88	0.277
15	7.59	9.61	1.84	0.278
16	10.56	10.80	1.90	0.411
17	5.64	32.37	1.92	0.834

Table A.34: List of fragments size and mass for Alu-P-D14-t2-F4.

Fragment	L_θ (mm)	L_z (mm)	t (mm)	m (g)
1	6.32	7.99	1.84	0.120
2	5.34	10.33	1.88	0.198
3	6.88	12.08	1.70	0.222
4	5.19	12.76	1.85	0.210
5	7.52	12.21	1.82	0.322
6	5.87	11.35	1.85	0.206
7	5.32	12.16	1.95	0.224
8	3.76	14.15	1.84	0.203
9	8.99	8.15	1.92	0.284
10	9.60	9.16	1.86	0.373
11	6.17	14.33	1.85	0.361
12	5.27	20.21	1.76	0.411
13	4.78	21.14	1.86	0.495
14	5.44	27.49	1.89	0.529

References

Altynova, M., Hu, X., Daehn, G.S., 1996. Increased ductility in high velocity electromagnetic ring expansion. Metallurgical and Materials Transactions A 27, 1837–1844.

Avizo, 2021. Version 2021.1, Thermofisher Scientific.

Cliche, N., Ravi-Chandar, K., 2018. Dynamic strain localization in magnesium alloy AZ31B-O. Mechanics of Materials 116, 189 – 201. IUTAM Symposium on Dynamic Instabilities in Solids.

Diep, Q.B., Moxnes, J.F., Nevstad, G., 2004. Fragmentation of projectiles and steel rings using numerical 3D simulations, in: The 21th International Symposium of Ballistics, Adelaide, Australia.

Feldkamp, L.A., Davis, L.C., Kress, J.W., 1984. Practical cone-beam algorithm. J. Opt. Soc. Am. A 1, 612–619.

Fressengeas, C., Molinari, A., 1985. Inertia and thermal effects on the localization of plastic flow. Acta Metallurgica 33, 387–396.

Fressengeas, C., Molinari, A., 1994. Fragmentation of rapidly stretching sheets. European Journal of Mechanics A/Solids 13, 251–268.

Goto, D., Becker, R., Orzechowski, T., Springer, H., Sunwoo, A., Syn, C., 2008. Investigation of the fracture and fragmentation of explosively driven rings and cylinders. International Journal of Impact Engineering 35, 1547–1556.

Grady, D.E., Benson, D.A., 1983. Fragmentation of metal rings by electromagnetic loading. Experimental Mechanics 12, 393–400.

Grady, D.E., Olsen, M.L., 2003. A statistics and energy based theory of dynamic fragmentation. International Journal of Impact Engineering 29, 293–306.

Hill, R., 1952. On discontinous plastic states, with special reference to localized necking in thin sheets. Journal of the Mechanics and Physics of Solids 1, 19–30.

Hiroe, T., Fujiwara, K., Hata, H., Takahashi, H., 2008. Deformation and fragmentation behaviour of exploded metal cylinders and the effects of wall materials, configuration,explosive energy and initiated locations. International Journal of Impact Engineering 35, 1578–1586.

Janiszewski, J., 2012. Ductility of selected metals under electromagnetic ring test loading conditions. International Journal of Solids and Structures 49, 1001–1008.

Kobryn, P.A., Moore, E.H., Semiatin, S.L., 2000. The effect of laser power and traverse speed on microstructure, porosity, and build height in laser-deposited Ti-6Al-4V. Scripta Materialia 43, 299–305.

Koutiri, I., Pessard, E., Peyre, P., Amlou, O., De Terris, T., 2018. Influence of slm process parameters on the surface finish, porosity rate and fatigue behavior of as-built Inconel 625 parts. Journal of Materials Processing Technology 255, 536–546.

Laursen, C.M., DeJong, S.A., Dickens, S.M., Exil, A.N., Susan, D.F., Carroll, J.D., 2020. Relationship between ductility and the porosity of additively manufactured AlSi10Mg. Materials Science and Engineering: A 795, 139922.

Marvi-Mashhadi, M., Vaz-Romero, A., Sket, F., Rodríguez-Martínez, J.A., 2021. Finite element analysis to determine the role of porosity in dynamic localization and fragmentation: Application to porous microstructures obtained from additively manufactured materials. International Journal of Plasticity 143, 102999.

Materialise, 2022. Materialise NV, Belgium.

Mercier, S., Granier, N., Molinari, A., Llorca, F., Buy, F., 2010. Multiple necking during the dynamic expansion of hemispherical metallic shells, from experiments to modelling. Journal of the Mechanics and Physics of Solids 58, 955–982.

Mercier, S., Molinari, A., 2003. Predictions of bifurcations and instabilities during dynamic extensions. International Journal of Solids and Structures 40, 1995–2016.

Mercier, S., Molinari, A., 2004. Analysis of multiple necking in rings under rapid radial expansion. International Journal of Impact Engineering 30, 403–419.

Mott, N.F., 1947. Fragmentation of shell cases. Proceedings of the Royal Society of London. Series A. Mathematical and Physical Sciences 189, 300–308.

Nalli, F., Cortese, L., Concli, F., 2021. Ductile damage assessment of Ti6Al4V, 17-4PH and AlSi10Mg for additive manufacturing. Engineering Fracture Mechanics 241, 107395.

Neel, C., Sable, P., Flater, P., Lacina, D., 2020. Conical impact fragmentation test (CIFT). International Journal of Impact Engineering 140, 103540.

Niordson, F.L., 1965. A unit for testing materials at high strain rates. Experimental Mechanics 5, 29–32.

Rao, P., Painter, J., Appleby-Thomas, G., Critchley, R., Wood, D., Roberts, A., Hazael, R., 2020. Fragmentation studies by non-explosive cylinder expansion technique. International Journal of Impact Engineering 146, 103714.

Schneider, C.A., Rasband, W.S., Eliceiri, K.W., 2012. Nih image to imagej: 25 years of image analysis. Nat Meth 9, 671–675.

Slicer, 2022. Brigham and Women's Hospital (BWH).

Wesenberg, D., Sagartz, M., 1977. Dynamic fracture of 6061-T6 aluminium cylinders. Journal of Applied Mechanics 44, 643–646.

Zhang, H., Ravi-Chandar, K., 2006. On the dynamics of necking and fragmentation - I. Real-time and post-mortem observations in Al 6061-O. International Journal of Fracture 142, 183–217.

Zhang, H., Ravi-Chandar, K., 2008. On the dynamics of necking and fragmentation - II. Effect of material properties geometrical constraints and absolute size. International Journal of Fracture 150, 3–36.

Zhang, H., Ravi-Chandar, K., 2010. On the dynamics of localization and fragmentation - IV. Expansion of Al 6061-O tubes. International Journal of Fracture 163, 41–65.